

Research Article

Diachronous initiation of post-collisional magmatism in the Arabia-Eurasia collision zone



Yu-Chin Lin ^a, Sun-Lin Chung ^{a,b,*}, A. Feyzi Bingöl ^c, Liekun Yang ^d, Avtandil Okrostsvaridze ^e, Kwan-Nang Pang ^b, Hao-Yang Lee ^b, Te-Hsien Lin ^a

^a Department of Geosciences, National Taiwan University, Taipei, Taiwan

^b Institute of Earth Sciences, Academia Sinica, Taipei, Taiwan

^c Department of Geological Engineering, Firat University, Elazığ, Turkey

^d Institute of Geology and Geophysics, Chinese Academy of Sciences, Beijing, China

^e Institute of Earth Sciences, Ilia State University, Tbilisi, Georgia

ARTICLE INFO

Article history:

Received 1 October 2019

Received in revised form 20 January 2020

Accepted 20 January 2020

Available online 23 January 2020

Keywords:

Post-collisional magmatism

CIA volcanic province

Diachronous initiation

Bimodal composition

Oblique collision

Arabia

Eurasia

ABSTRACT

The continental collision between Arabia and Eurasia which gave rise to the Caucasus-Iran-Anatolia (CIA) volcanic province provides a unique opportunity for understanding collisional zone magmatism. This study reports a comprehensive dataset of ages and geochemical compositions of volcanic rocks formed during the initial phase of post-collisional magmatism in the CIA province. The age data indicate a diachronous onset of volcanism that began ~17 Ma in SE Anatolia, and propagated northward from ~11 to 9 Ma toward NE Anatolia and NW Iran. The rocks are characteristically bimodal, with dominantly basic ($\text{SiO}_2 = 48\text{--}52\text{ wt\%}$) and silicic ($\text{SiO}_2 = 58\text{--}71\text{ wt\%}$) components that feature significant isotopic variations ($\epsilon\text{Nd} = +6\text{ to }-5$), suggesting two principal magma sources: (1) a juvenile mantle-derived component, and (2) an older continental crust component. We therefore attribute the volcanic initiation to a migrating post-collisional extension regime caused by the successive breakoff of subducted Neo-Tethyan slabs. Subsequent volcanism that began from ~6.5 Ma resulted in a wide spectrum of calc-alkaline and alkaline rocks, with mafic to felsic lithologies in the entire province. From ~2 Ma, volcanism ceased in the western CIA province, and started propagating eastward and southeastward to SE Iran, following the Urumieh-Dokhtar magmatic belt, consistent with the notion of an oblique continental collision between Arabia and Eurasia.

© 2020 Elsevier B.V. All rights reserved.

1. Introduction

Collision zone magmatism is common on Earth. Typical examples are found all along the 7000-km-long Alpine-Himalayan orogenic belt, and are the result of continental collisions of the African, Arabian and Indian plates with the Eurasian margin (Şengör, 1984). In its central segment the collision between Arabia and Eurasia, starting possibly from the latest Eocene (Allen and Armstrong, 2008; McQuarrie and van Hinsbergen, 2013), led to formation of the Turkish-Iranian Plateau. This collision zone is associated with widespread “post-orogenic” (Turner et al., 1992) or “post-collisional” (Chung et al., 2005; Pearce et al., 1984; Şengör and Kidd, 1979) volcanic eruptions that have attracted a wide range of petrogenetic and tectonic studies (e.g., Dilek et al., 2010; Keskin, 2003; Lin et al., 2020; Neill et al., 2015; Nikogosian et al., 2018; Pang et al., 2013; Pearce et al., 1990; Rabayrol

et al., 2019; Schleiffarth et al., 2018). Eruptions took place from the Miocene to Quaternary, primarily within the Lesser Caucasus, NW Iran and eastern Anatolia (Fig. 1), herewith referred to as the Caucasus-Iran-Anatolia (CIA) volcanic province. A fundamental issue that remains unresolved in understanding the history of this region is the initiation of volcanism that led to the observed spatial and temporal distribution of this vast volcanic province.

Therefore, this study aims to (1) present a comprehensive dataset of ages and geochemical compositions of the initial phase of post-collisional volcanic rocks exposed in the CIA province; (2) establish the spatial and temporal distribution of the initial volcanism; (3) better constrain the magma sources and petrogenetic processes; and (4) explore broader tectonic implications by synthesizing literature data of other magmatic rocks from the Arabia-Eurasia collision zone.

2. Geologic background

The Arabia-Eurasia collision zone results from a Turkic-type orogeny (Şengör et al., 2008), which is characterized by complex subduction, accretion and collision processes among a number of micro-continents.

* Corresponding author at: Institute of Earth Sciences, Academia Sinica, Taipei 11529, Taiwan.

E-mail address: sunlin@ntu.edu.tw (S.-L. Chung).

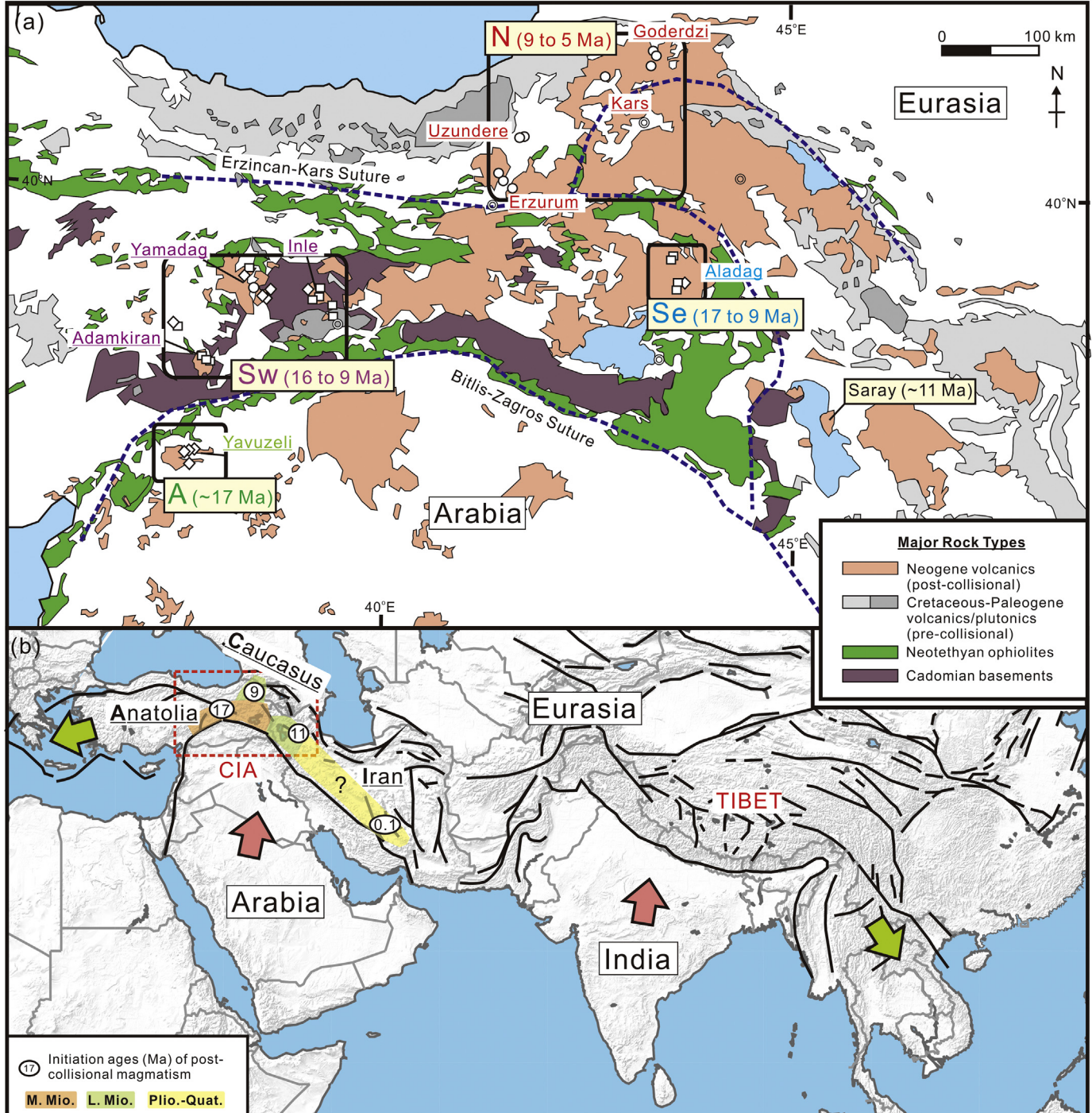


Fig. 1. (a) A simplified geologic map of magmatic rocks in the Caucasus-Iran-Anatolia (CIA) province (modified after Aghanabati, 1993). Studied rocks are collected from four zones marked with age spans of the initial stage of volcanism postdating the Arabia-Eurasia collision. (b) Map of the Arabia-India-Eurasia collision zone, with principal faults (black lines) and initiation ages of the CIA post-collisional magmatism (this study; Chiu et al., 2013; Pang et al., 2013; Pang et al., 2015). Green arrows indicate directions of the continental extrusion caused by the northward indentation of Arabia and India (pink arrows). (For interpretation of the references to colour in this figure legend, the reader is referred to the web version of this article.)

The micro-continents, rifted from Gondwanaland and of ribbon-shaped, started accreting to the Eurasian or Arabian margins since the Jurassic (Şengör, 1984; Stampfli and Borel, 2002). They are exposed now as the Cadomian basement rocks in the region (Fig. 1), best exemplified by the Bitlis-Purge massif, the Tauride massif and the Sanandaj-Sirjan belt, and date from ~600 to 540 Ma (Beyarslan et al., 2016; Shafaii Moghadam et al., 2015; Ustaömer et al., 2009). The closure of the Neo-Tethys gave rise to the emplacement of ophiolitic mélange

along two principal suture zones, i.e., the Bitlis-Zagros in the south and the Erzincan-Kars in the north (Fig. 1a). Before that, the Neo-Tethyan subduction system around the CIA volcanic province resulted in widespread arc magmatic rocks from the Cretaceous to the Paleogene.

Most workers believe that the final collision of Arabia with Eurasia occurred between 35 and 20 Ma (Allen and Armstrong, 2008; McQuarrie and van Hinsbergen, 2013). The collision, or the

closure of the Neo-Tethys, however, may have occurred diachronously along the Bitlis-Zagros suture zone because of the oblique contact between the two continents (Chiu et al., 2013; McQuarrie and van Hinsbergen, 2013). Post-collisional igneous rocks occur widely in the entire collision zone but, as mentioned above, prevail in the CIA province where volcanic successions of up to ~1 km thickness are exposed in some localities (Fig. 2). The initiation of this voluminous post-collisional magmatism in space and time remains controversial, with suggestions of initial volcanic eruptions at ~11 Ma in the Erzurum-Kars plateau (Keskin, 2003; Keskin et al., 1998), ~15 Ma in the northern Van area (Lebedev et al., 2010), and ~11 Ma in NW Iran (Pang et al., 2013). Most studies have instead focused on the younger and more widespread stage of volcanism in the province that occurred from the Pliocene to Quaternary, thus yielding various geodynamic models responsible for the magma generation. Among these, the two most popular models are “wholesale” delamination of the thickened lithospheric mantle (Pearce et al., 1990) and rollback and breakoff of the subducted Tethyan oceanic slab (Keskin, 2003; and refs. therein).

3. Rationale and samples

The CIA volcanic province has been widely investigated in various aspects, and its general age distribution, field occurrence, and petrologic and geochemical characteristics have already been documented (e.g., Ercan et al., 1990; Keskin et al., 1998; Pearce et al., 1990; Yilmaz et al., 1987). This study focuses on some specific regions where volcanic successions of the initial stage of post-collisional magmatism are exposed (Figs. 1–4). A total of forty-eight samples reported in this paper were recovered from four specific areas, including one in the Arabian foreland and three from other eastern Anatolian volcanic fields (Fig. 1a). Four simplified stratigraphic columns (Fig. 2) are depicted to illustrate the pertinent volcanic successions and sampling positions, together with representative field photos of selected outcrops (Fig. 3). Additional descriptions of the sample localities are as follows.

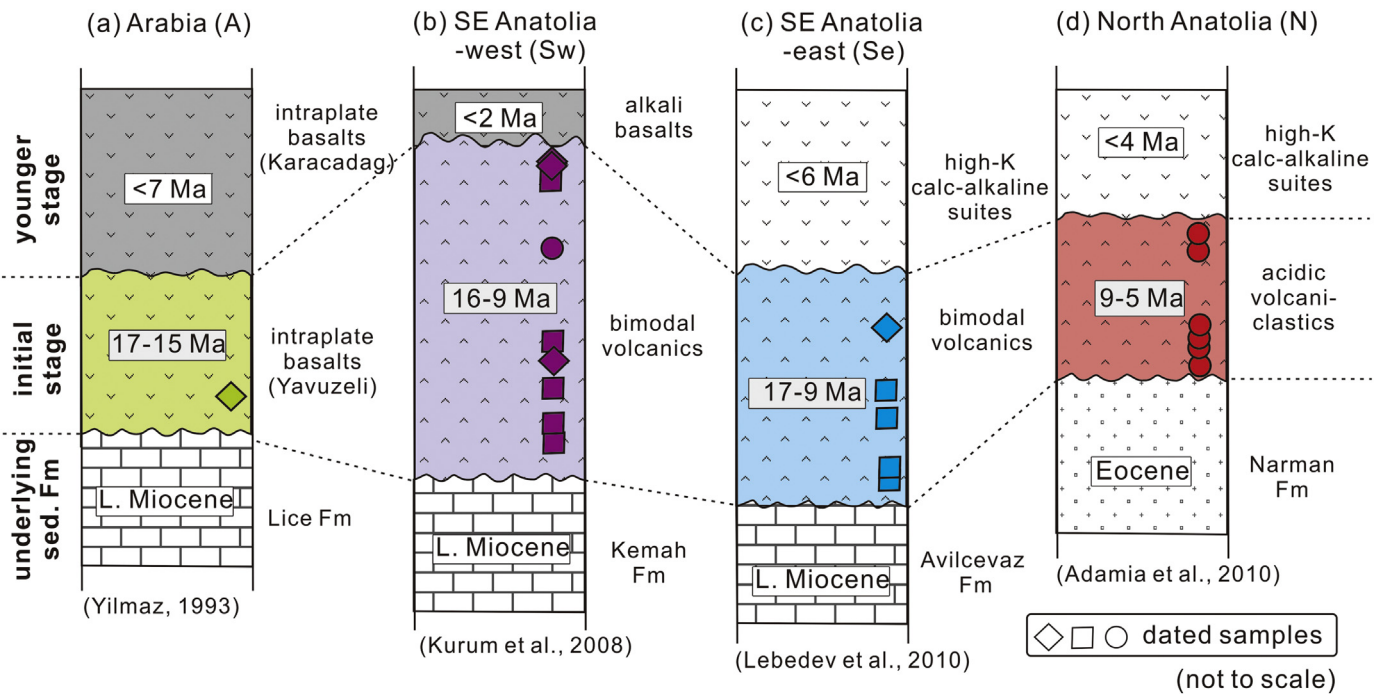


Fig. 2. (a)–(d) Simplified geologic columnar sections (not to scale) of sample localities based on field observation and literature information (Adamia et al., 2010; Keskin et al., 1998; Kürüm et al., 2008; Lebedev et al., 2010; Yilmaz, 1993). Formations are shown in three parts, from lower to upper: underlying sedimentary formation, and the initial stage and younger stage of the post-collisional volcanic sequences. This study focuses on the initial stage, in which dated samples are marked.

3.1. Arabian foreland (zone A)

The Arabian foreland located in the south of the Bitlis-Zagros suture zone has a basement composed mainly of Precambrian rocks, overlain with a thick pile of shallow water sedimentary formations of early Paleozoic to Miocene ages (Sengör et al., 2008; and refs. therein). Intraplate basalts are widespread in the region, with many outcrops resting on a Lower Miocene limestone, even though these basalts are dominantly Pliocene to Quaternary in age (Lustrino et al., 2010). Among the oldest eruptions that have been documented include the Yavuzeli basalts, dated at ~19–16 Ma by the K–Ar method (Figs. 1a and 2a) (Arger et al., 2000). These basalts are typical of intraplate or OIB-type geochemical compositions and have been studied extensively for their petrogenesis (Arger et al., 2000; Lustrino et al., 2010; Nikogosian et al., 2018). In this study, we collected five basaltic lava samples from the Yavuzeli basalts (Fig. 2a), with one from the lower part (Fig. 3a) being dated using the Ar–Ar method.

3.2. Adamkiran-Yamadag-Inle volcanic field (SE Anatolia-west, zone SW)

Thick initial stage volcanic successions outcrop in the western part of SE Anatolia (Figs. 1a and 2b), where we performed a field survey with systematic sampling from three main volcanic fields: (1) Adamkiran (Fig. 3b), (2) Yamadag (Fig. 3c) and (3) Inle (Fig. 3d). This region is widely underlain by Cadomian basement rocks (Fig. 1a), covered unconformably with limestone or sedimentary rocks of various ages (Figs. 2b and 3). A total of twenty-two volcanic samples, including six basic and sixteen silicic rocks, were collected from this region. Note that Ar–Ar age data (~15.8 to 8.9 Ma) are available for the volcanic successions in the Yamadag area, which consist of volcaniclastic basaltic rocks from the bottom, flows of basalt and dacite in the middle, and alkali basaltic flows on the top (Kürüm et al., 2008).

3.3. Aladag-Van volcanic field (SE Anatolia-east, zone SE)

Volcanic successions of the initial stage also crop out in the eastern part of SE Anatolia (Fig. 1a). Like those in the Aladag and Van

3.4. North Anatolia (N)

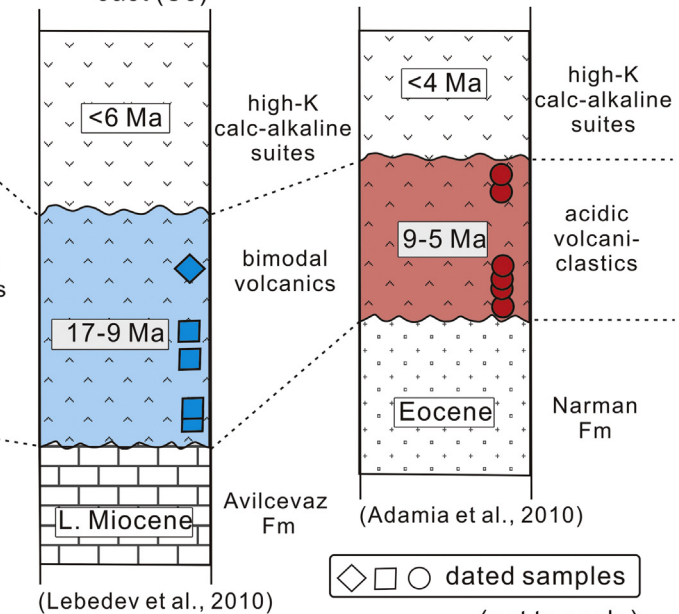


Fig. 2. (a)–(d) Simplified geologic columnar sections (not to scale) of sample localities based on field observation and literature information (Adamia et al., 2010; Keskin et al., 1998; Kürüm et al., 2008; Lebedev et al., 2010; Yilmaz, 1993). Formations are shown in three parts, from lower to upper: underlying sedimentary formation, and the initial stage and younger stage of the post-collisional volcanic sequences. This study focuses on the initial stage, in which dated samples are marked.

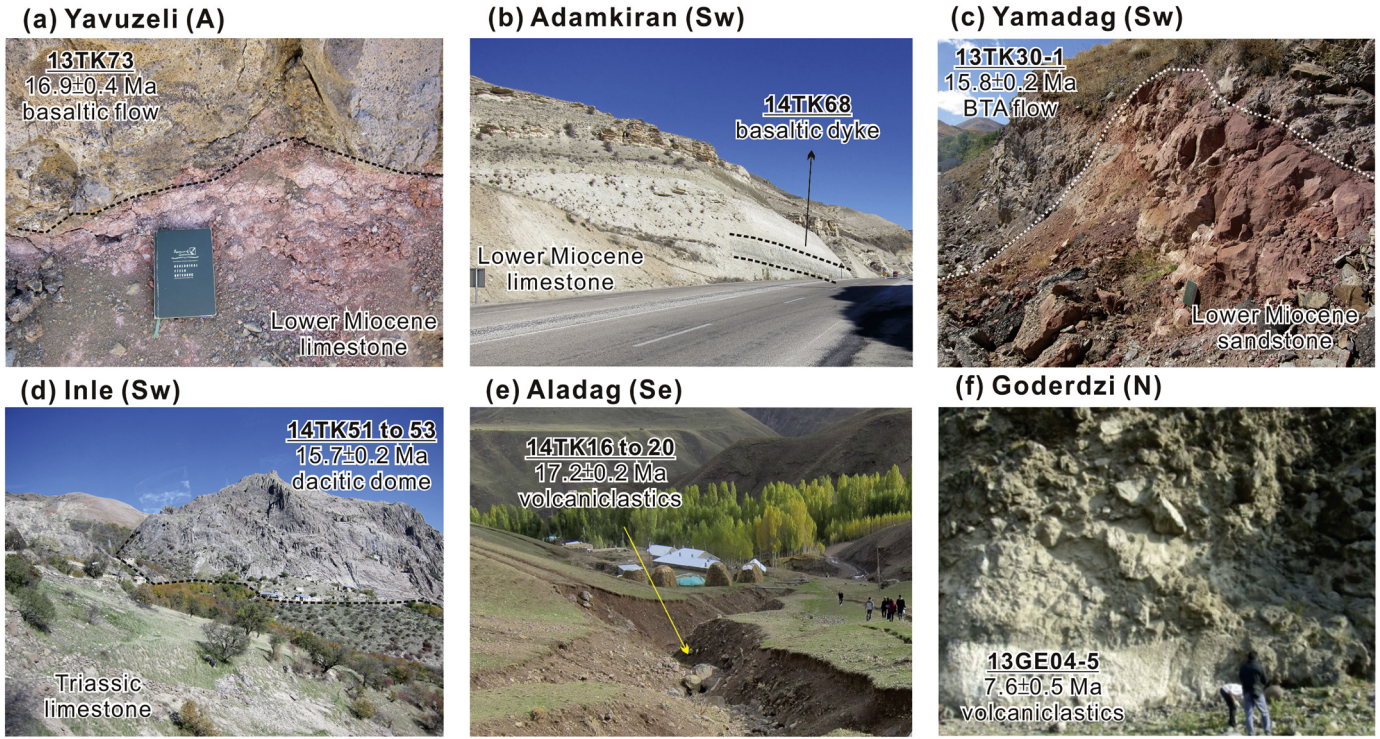


Fig. 3. Representative field photos: (a) the Yavuzeli basaltic lava flow, underlain by the Lower Miocene limestone, (b) the middle Miocene basaltic dyke in Adamkiran, intruding to the Lower Miocene limestone, (c) a basaltic trachyandesitic flow in Yamadag, covering on the Lower Miocene sandstone, (d) a dacitic dome overlying the Triassic limestone in Inle, (e) volcanioclastics from a dry river bed in Aladag area, and (f) a volcanioclastic fragment from the Goderdzi formation of southern Georgia.

volcanic fields (Lebedev et al., 2010; Yilmaz et al., 1987), eruptions overlie the Lower Miocene Avilcevaz formation (Fig. 2c). The volcanism appears to have lasted from the Middle Miocene to Quaternary based on K—Ar ages (Lebedev et al., 2010). Our new and unpublished data enable us to further divide the rock sequences into two main stages, an earlier one (~17–9 Ma) and a later one (~6–0 Ma), with a magmatic gap or quiescence time in between (Lin, 2020, PhD thesis in prep.). This paper presents dating results of seven volcanic samples from the earlier stage, among which an oldest zircon U—Pb age of 17.2 ± 0.2 Ma is obtained from Aladag volcanioclastics (Fig. 3e).

3.4. Erzurum-Kars volcanic field (NE Anatolia, zone N)

In NE Anatolia, the Erzurum-Kars plateau overlies vast Eocene volcanic sequences that represent the upper part of the Cretaceous-Paleogene igneous complex in the Pontides block-South Armenian block (Figs. 1a and 4). This study focuses on two overlying volcanic fields, near the Erzurum and Kars-Goderdzi areas (Fig. 4). The Erzurum successions were divided by Keskin et al. (1998) into three volcanic stages: (1) basal volcanioclastic rocks from 11 to 6 Ma, (2) dacitic lavas from 6 to 5 Ma, and (3) bimodal igneous activity from 5 to 1.5 Ma. The basal volcanioclastic rocks in the Kars area, e.g., the lower sequence in Aras, may extend northward to Goderdzi, S. Georgia (Fig. 3f) where K—Ar ages of ~9–7 Ma have been documented repeatedly in regional studies (Adamia et al., 2010; Lebedev et al., 2012). The Goderdzi basal succession is overlain by the plateau sequence which consists of calc-alkaline rocks from ~3.5 Ma to Recent and extends to the eastern part, suggesting an eastward migration of volcanism. This paper reports: (1) seven andesitic to dacitic lavas from the earlier two stages in the Erzurum-Uzundere area and (2) seven andesitic to rhyolitic pyroclastics from the basal succession in the Kars-Goderdzi area near the Turkish-Georgian border.

4. Analytical methods

Twenty silicic samples were dated by the zircon U—Pb method, using an Agilent 7500s ICP-MS coupled with a Photon-Machines 193 nm laser ablation system at the Department of Geosciences, National Taiwan University following the analytical procedures reported in Chiu et al. (2013). Cathodoluminescence (CL) images were taken to inspect the internal textures of zircon grains and to select suitable positions for in-situ U—Pb analyses. Most zircons in this study are euhedral with long prismatic pyramidal forms and show oscillatory zoning, indicating magmatic origins. The zircon U—Pb results and representative CL images are illustrated in Fig. A1, and the analytical dataset is given in Table A1 (supplementary material #1).

Three basic samples, which did not crystallize zircons, and two silicic samples were subjected to whole-rock Ar—Ar dating analyses using a Noblesse mass spectrometer and lab facilities at IGGCAS, Beijing. The detailed instrumentation and analytical procedures have been described in Wang et al. (2014). The Ar—Ar results are listed in Table A2 and plateau age diagrams are given in Fig. A2 (supplementary material #2).

Forty-eight fresh samples were selected and powdered for whole-rock geochemical analysis. Major elements were measured on fused glass beads using a Rigaku® RIX 2000 XRF spectrometer, with loss-on-ignition obtained by routine procedures. Trace elements were analyzed by the dissolution of the same glass beads using an Agilent 7500cs quadrupole ICP-MS. The analytical details of major and trace element analyses can be found in Lin et al. (2012). The international standards results for AGV-2, BCR-2, BHVO-2, and DNC-1, measured together with the samples are given in Table A3-1 (supplementary material #3). Fourteen samples were selected for Sr—Nd isotopic analyses using a Nu Plasma II multi-collector ICP-MS. The international standards SRM987 and JNd-1 were used for normalization. Long term mean values of the Sr and Nd standards of the laboratory during the measurement period are $^{87}\text{Sr}/^{86}\text{Sr} = 0.710311 \pm 32$ (2σ , $n = 19$) and $^{143}\text{Nd}/^{144}\text{Nd} =$

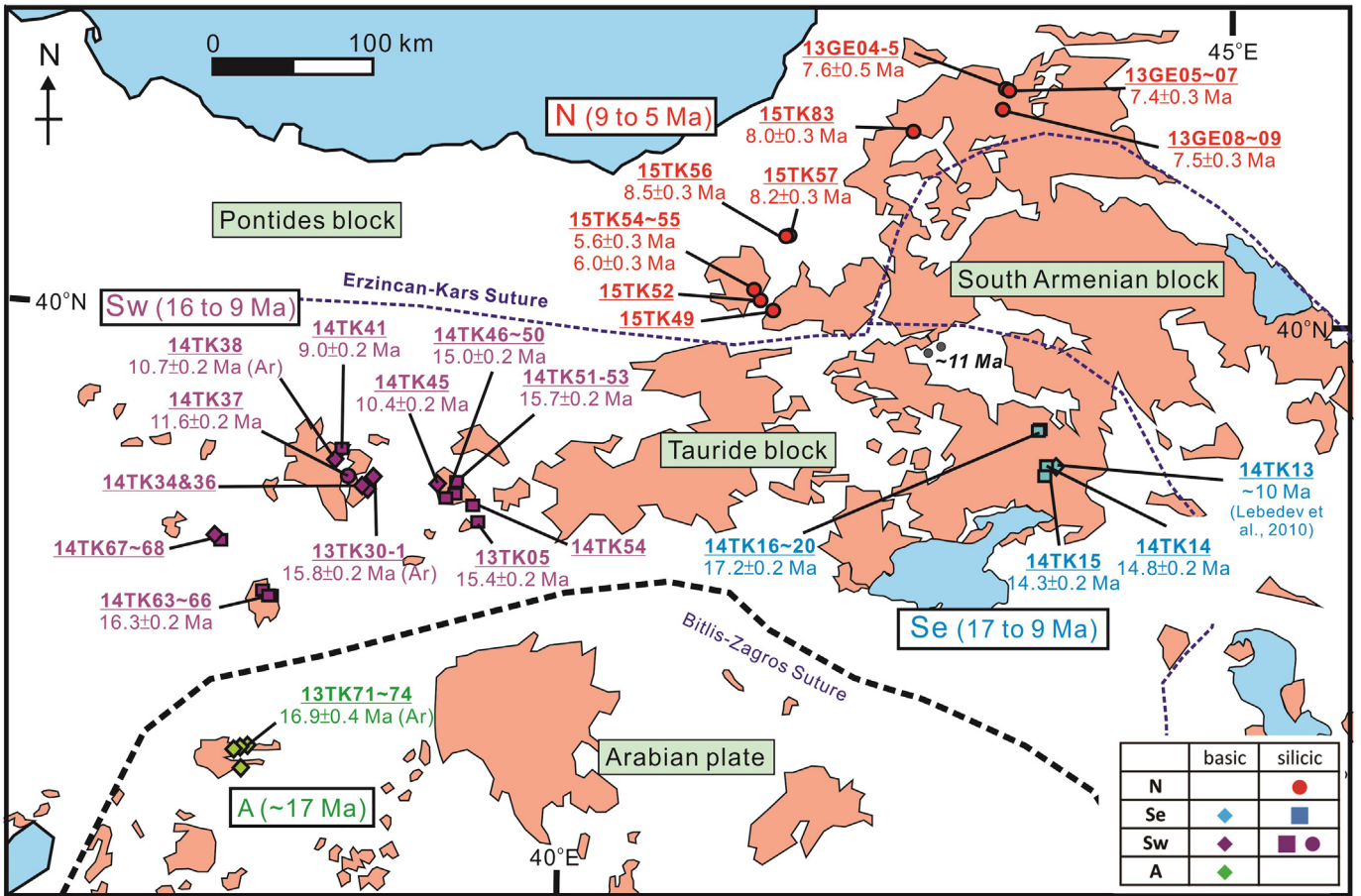


Fig. 4. Summary of age data of the initial stage of volcanic rocks in the CIA province, from Arabia, SE Anatolia (western and eastern parts), and NE Anatolia, with names and boundaries of the main terranes shown. The ~11 Ma in italics represents one of the basal age obtained by Keskin et al. (1998) and Ercan et al. (1990).

0.512097 ± 18 (2σ , $n = 66$) (Table A3–2; supplementary material #3). The analytical details have been described in Lee et al. (2012).

5. Results

5.1. Geochronology

Our zircon U—Pb and whole-rock Ar—Ar dating results are summarized together with literature data in Table 1, which are plotted in terms of the outcrop localities in Fig. 4 and the distance from the Bitlis-Zagros Suture in Fig. 5. The age data suggest a diachronous distribution of the initial volcanic phase in the CIA province (see next section). Below we briefly describe our age results from different volcanic zones (Table 1).

Zone A (~17 Ma): our Ar—Ar age result (16.9 ± 0.4 Ma) of a basalt sample 13TK72-2 is broadly coeval with K—Ar ages reported by Arger et al. (2000).

Zone Sw (16–9 Ma): we report zircon U—Pb ages of six silicic samples, and Ar—Ar ages of two silicic and two basic samples from this zone, with a silicic sample (13TK05) being dated by two methods that gave an identical age of 15.4 ± 0.2 Ma. In addition to the magmatic zircons that yielded mean $^{206}\text{Pb}/^{238}\text{U}$ ages from 16.3 to 9.0 Ma (Fig. A1), the silicic samples contain inherited zircons (18 out of 119 dated grains) with ages varying from the Neoproterozoic (705–595 Ma, $n = 4$), Cambrian (453–435 Ma, $n = 2$), and Late Cretaceous (71 Ma, $n = 2$) to the Oligo-Miocene (25–13 Ma, $n = 10$) (Table A1). The Ar—Ar ages range from 15.8 to 10.4 Ma (Fig. A2).

Zone Se (17–9 Ma): five silicic samples yielded zircon U—Pb ages from 17.2 to 14.3 Ma (Fig. A1). Some inherited zircons were observed (17 out of 119 dated grains) from the northern Aladag volcaniclastics,

with ages ranging from the Neoproterozoic (886–606 Ma, $n = 3$), Paleozoic (491–285 Ma, $n = 8$), and Early Cretaceous (137 Ma, $n = 1$) to the Late Eocene-Early Miocene (39–21 Ma, $n = 5$) (Table A1). Given that we failed to obtain any age result of basic rocks in this zone, an inferred age of ~10 Ma is assumed for the basalt sample 14TK13, according to the K—Ar date of 9.9 ± 0.3 Ma reported for basalt from the nearby area by Lebedev et al. (2010).

Zone N (9–5 Ma): nine silicic samples yielded zircon U—Pb ages from 8.5 to 5.6 Ma (Fig. A1). Inherited zircons (9 out of 177 dated grains) exist only in samples from the Uzundere field, with ages from the Carboniferous (324 Ma, $n = 1$), Jurassic (182–163 Ma, $n = 6$), Late Cretaceous (95 Ma, $n = 1$) and Eocene (45 Ma, $n = 1$) (Table A1).

5.2. Geochemistry

The overall data indicate a bimodal composition of the initial volcanic phase in the CIA province (Fig. 6), best exemplified by Zones Sw and Se from which both basic and silicic rocks that are well-exposed, and were collected in this study (Table 2). In contrast, only basic rocks exist in Zone A, and only silicic samples were recovered from Zone N (Fig. 6). We note however that some studies have reported the associated occurrence of basic volcanic rocks in the transition zone between Zone Se and Zone N (Ercan et al., 1990; Keskin et al., 1998) that belong to Zone Se in this study (Fig. 4 and supplementary material #4). All the basic samples are of basaltic composition with a limited SiO₂ range from 45.7 to 51.4 wt%, whereas the silicic samples vary from andesitic to rhyolitic with SiO₂ ranging from 58.3 to 70.7 wt%, and showing a gap between 52 and 58 wt% SiO₂ (Fig. 6). The only exception is a basaltic andesite sample (13TK30-1, 15.8 ± 0.2 Ma) that has SiO₂ = 54.7 wt%

Table 1

Summary of age data reported for the initial phase of the post-collisional volcanic rocks from the CIA province.

Locality	Sample	Rock type	Method	Age (Ma $\pm 2\sigma$)	Reference
Arabia (A)					
Yavuzeli	13TK72-2	Basalt	Ar-Ar (gm)	16.9 \pm 0.4	This study
Yavuzeli	K1	Basalt	K-Ar (wr)	16.5 \pm 0.3	Arger et al. (2000)
Yavuzeli	X	Basalt	K-Ar (wr)	17.1 \pm 0.4	Arger et al. (2000)
Yavuzeli	T	Basalt	K-Ar (wr)	18.6 \pm 0.4*	Arger et al. (2000)
SE Anatolia-west (Sw)					
Yamadag	13TK30-1	Basaltic trachyandesite	Ar-Ar (gm)	15.8 \pm 0.2	This study
Yamadag	14TK37-1	Dacite	U-Pb (zc)	11.6 \pm 0.2	This study
Yamadag	14TK38	Basalt	Ar-Ar (gm)	10.7 \pm 0.2	This study
Yamadag	14TK41	Dacite	U-Pb (zc)	9.0 \pm 0.2	This study
Yamadag	AV79	Dacite	Ar-Ar (bi)	15.1 \pm 0.1	Kürüm et al. (2008)
Yamadag	AV80	Basalt	Ar-Ar (gm)	15.8 \pm 0.2	Kürüm et al. (2008)
Yamadag	AV83	Dacite	Ar-Ar (amp)	12.2 \pm 0.2	Kürüm et al. (2008)
Inle	13TK05	Dacite	U-Pb (zc)	15.4 \pm 0.2	This study
"	"	"	Ar-Ar (gm)	15.4 \pm 0.2	This study
Inle	14TK45	Basalt	Ar-Ar (gm)	10.4 \pm 0.2	This study
Inle	14TK46	Dacite	U-Pb (zc)	15.0 \pm 0.2	This study
Inle	14TK51	Trachyandesite	U-Pb (zc)	15.7 \pm 0.2	This study
Adamkiran	14TK64	White tuff	U-Pb (zc)	16.3 \pm 0.2	This study
Kepez	K-4	Trachybasalt	Ar-Ar (wr)	14.0 \pm 0.3	Ekici (2016)
Kepez	K-14	Dacite	Ar-Ar (wr)	15.3 \pm 0.2	Ekici (2016)
Kepez	K-31	Basaltic trachyandesite	Ar-Ar (wr)	14.1 \pm 0.2	Ekici (2016)
Kepez	K-58	Basalt	Ar-Ar (wr)	13.6 \pm 0.2	Ekici (2016)
Orduzu	OV8	Basaltic trachyandesite	Ar-Ar (pl)	16.0 \pm 0.1	Onal et al. (2018)
Orduzu	OV20	Rhyolite	Ar-Ar (pl)	16.2 \pm 0.1	Onal et al. (2018)
SE Anatolia-east (Se)					
Aladag	14TK14	Andesite	U-Pb (zc)	14.8 \pm 0.2	This study
Aladag	14TK15	Andesite	U-Pb (zc)	14.3 \pm 0.2	This study
Aladag	14TK16	Andesite	U-Pb (zc)	17.2 \pm 0.2	This study
Aladag	14TK18	Dacite	U-Pb (zc)	17.2 \pm 0.2	This study
Aladag	14TK20	Andesite	U-Pb (zc)	17.2 \pm 0.2	This study
Aladag	08-102	Basalt	K-Ar (wr)	9.9 \pm 0.3	Lebedev et al. (2010)
Aladag	08-113	Andesite	K-Ar (wr)	14.9 \pm 0.3	Lebedev et al. (2010)
NE Anatolia (N)					
Erzurum	15TK54	Andesite	U-Pb (zc)	5.6 \pm 0.3	This study
Erzurum	15TK55	Andesite	U-Pb (zc)	6.0 \pm 0.3	This study
Uzundere	15TK56	Dacite	U-Pb (zc)	8.5 \pm 0.3	This study
Uzundere	15TK57	Dacite	U-Pb (zc)	8.2 \pm 0.3	This study
Kars	15TK83	Dacite	U-Pb (zc)	8.0 \pm 0.3	This study
Goderdzi	13GE04-5	Trachyte	U-Pb (zc)	7.6 \pm 0.5	This study
Goderdzi	13GE05-2	Rhyolite	U-Pb (zc)	7.4 \pm 0.3	This study
Goderdzi	13GE06	Dacite	U-Pb (zc)	7.5 \pm 0.2	This study
Goderdzi	13GE08	Trachyte	U-Pb (zc)	7.5 \pm 0.3	This study
Goderdzi	YuG-164	trachydacite	K-Ar (gm)	7.8 \pm 0.2	Lebedev et al. (2012)
Transition zone between N and Sw-Se					
Cat	AG211	Dacite	K-Ar (gm)	8.3 \pm 0.1	Innocenti et al. (1982)
Cat	AG204	Dacite	K-Ar (gm)	7.8 \pm 0.2	Innocenti et al. (1982)
Kotek	MK138	Basaltic andesite	K-Ar (wr)	9.9 \pm 0.4	Keskin et al. (1998)
Kotek	K144	Basalt	K-Ar (wr)	11.1 \pm 0.5	Keskin et al. (1998)
Kosedag	KO1	Dacite	K-Ar (wr)	11.4 \pm 0.9	Ercan et al. (1990)
Karatepe	KA1	Dacite	K-Ar (wr)	11.2 \pm 1.5	Ercan et al. (1990)
Karatepe	AG5	Dacite	K-Ar (bi)	13.1 \pm 0.3	Innocenti et al. (1976)
NW Iran					
Saray	08-64	Leucite basanite	Ar-Ar (gm)	11.0 \pm 0.1	Pang et al. (2013)
Saray	08-75	Leucite tephrite	Ar-Ar (gm)	10.7 \pm 0.2	Pang et al. (2013)
Saray	110	Phonolite	U-Pb (zc)	10.6 \pm 0.2	Lechmann et al. (2018)
Saray	113	Tuff	U-Pb (zc)	10.7 \pm 0.3	Lechmann et al. (2018)
Khoy	60	Trachydacite	U-Pb (zc)	11.3 \pm 0.2	Lechmann et al. (2018)
Khoy	169	Andesite	U-Pb (zc)	13.6 \pm 0.3	Lechmann et al. (2018)
Takab	188	Dacite	U-Pb (zc)	10.6 \pm 0.2	Lechmann et al. (2018)
Ghorveh	PGV-2	Rhyolite	Ar-Ar (gm)	10.6 \pm 0.2	Azizi et al. (2014)

from the Yamadag field in Zone Sw (Table 1). This sample and a few basaltic andesites also reported from the Yamadag volcanic field (Kürüm et al. (2008) display similar incompatible trace element patterns with the associated basic rocks (Fig. 7) Hence, these are regarded as a more evolved member of the basic group. All the samples studied here can be classified as medium-K to high-K calc-alkaline suites (Fig. 6b).

Trace element characteristics are presented using rare earth element (REE) patterns and primitive mantle-normalized incompatible element

diagrams, or spidergrams (Fig. 7). The basic rocks from Zone A (Fig. 7a) are characterized by enrichment of light REE and slight or insignificant depletion in high field strength elements (Nb and Ta), similar to other OIB-type intraplate basalts from the Arabian foreland (Lustrino et al., 2010; Pearce et al., 1990; Shaw et al., 2003). In comparison, although the basic rocks from Zones Sw and Se have similar REE and spidergram patterns, they are also relatively depleted in Nb and Ta (Fig. 7b and c). All silicic rocks from Zones Sw, Se and N are characterized by significant

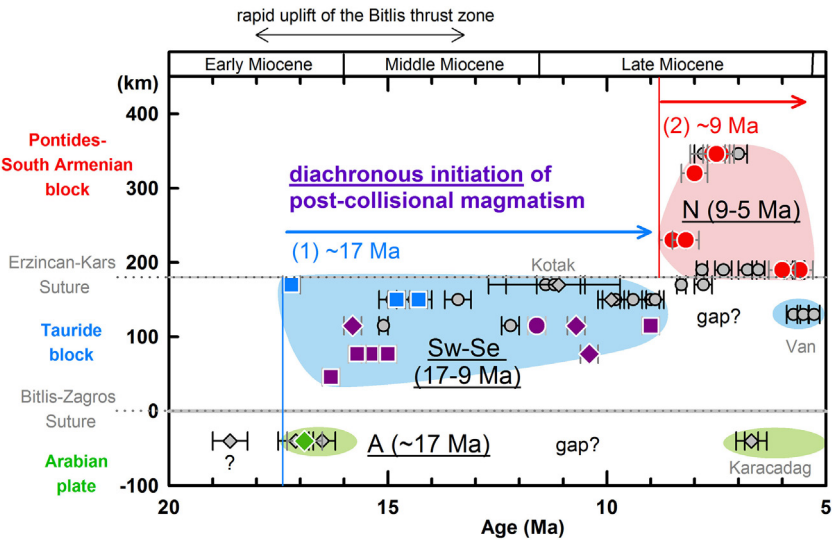


Fig. 5. Spatial and temporal variations observed in the CIA volcanic province. Our new data are plotted using colored symbols (refer to Fig. 6) and literature data in gray diamonds for basic rocks and circles for silicic rocks (Arger et al., 2000; Ercan et al., 1990; Keskin et al., 1998; Kürüm et al., 2008; Lebedev et al., 2010; Lustrino et al., 2010). The rapid uplift of the Bitlis thrust zone in 18–13 Ma is given by the apatite fission-track ages (Okay et al., 2010).

depletion in high field strength elements, coupled with enrichments in large-ion lithophile elements (Cs, Rb, Ba, K, Sr) and Pb (Fig. 7). Overall, rocks from the latter three zones have geochemical characteristics resembling those of Cretaceous to Paleogene magmatic rocks in the peri-Arabian region, and indicate the involvement of Tethyan subduction-metasomatized lithospheric mantle and associated crustal processes in their petrogenesis (Dilek et al., 2010; Keskin et al., 1998; Pearce et al., 1990).

All silicic rocks are LREE-enriched (Fig. 7), with no or moderately negative Eu anomalies ($\text{Eu}/\text{Eu}^* = 0.8\text{--}1.0$). They contain a generally similar abundance range in LREE but highly variable in heavy REE. More specifically, samples from Zone Se have the highest HREE ($>10\times$ chondrite) and those from Zone N have the lowest ($<10\times$ chondrite), implying that in Zone N specific minerals like garnet and/or amphibole may have played a role in magma generation (Castillo, 2012; Keskin et al., 1998). An exception is one rhyolite sample from Zone Sw (14TK37-1, Fig. 7b), which has the highest SiO_2 (70.7 wt%), and a U-shape REE pattern – indicative of amphibole fractionation, and a positive εNd value of +3.3 (Fig. 8).

The Sr–Nd isotopic data are listed in Table A3, with calculated εNd values versus SiO_2 contents plotted in Fig. 8. In Zone A, basalt sample (13TK-71) has a positive εNd value (+2.8) that is consistent with isotopic compositions of associated (albeit younger) intraplate basalts from nearby regions (Lustrino et al., 2010). Rocks from Zone Sw are characterized by more heterogeneous isotopic compositions, with basic samples having high, positive εNd values (+5.6 to +2.9, $n = 3$) and silicic samples varying from positive to negative εNd values (+3.3 of sample 14TK37-1 and –2.2 to –4.7, $n = 3$). The silicic rocks from Zone Se have exclusively negative εNd values (–3.3 and –5.0, $n = 2$), in contrast to those from Zone N that have only positive εNd values, true for both the Erzurum field (+1.7) or the Kars field (+3.1 to +4.1, $n = 3$).

6. Discussion

6.1. Diachronous initiation of the CIA volcanic province

Our new age results, combined with selected age data from the literature (Figs. 4 and 5), suggest a diachronous initiation of the post-collisional volcanism in the CIA province. As depicted in Fig. 5, the volcanism began at ~17 Ma in both Zones Se and A, and are broadly coevally (~16.3 Ma) in Zone Sw. Such an age distribution does not support a southward magmatic migration from the Erzincan-Kars Suture to the

Bitlis-Zagros Suture, as suggested by some studies (Keskin, 2003; Schleiffarth et al., 2018). Instead, the volcanism appears to have migrated northward from SE Anatolia to NE Anatolia, or more specifically, from the southern volcanic fields (Zones Sw and Se) in the Tauride block, to the northern volcanic field (Zone N) in the Pontides block–South Armenian block (Fig. 4). Eruptions in the north started from ~9 Ma and resulted in the second stage of initial volcanic rocks during 9–5 Ma when post-collisional volcanism in the southern province became less active or dormant (Fig. 5).

6.2. Significance of the bimodal volcanic suite

The compositional bimodality identified by this study lends support to a popular interpretation that associates the post-collisional magmatism within the CIA province with an extensional tectonic setting (Keskin, 2003; Pearce et al., 1990). Similar scenarios that involve post-collisional extension responsible for collision zone magmatism have been proposed not only along the Tethyan orogenic belt (Chung et al., 2005; Jolivet and Faccenna, 2000; Sengör, 1984) but worldwide (Li and Li, 2007; Thompson and Connolly, 1995; Zhu et al., 2012). In the CIA province, post-collisional extension may also have facilitated the initiation of strike-slip movement along with the Anatolian fault system, which accounts for regional and continental extrusion (Fig. 1b), and began in the middle Miocene (cf. Sengör et al., 2008; and refs. therein).

Moreover, the bimodal suite indicates different origins and source regions for the basic and silicic magmas. Under an extensional setting, the magmatic system was driven primarily by mantle-derived melts. To fingerprint the characteristics of the mantle sources, a Th/Yb-Nb/Yb projection is used after Pearce (2008). Enrichment of Th relative to the equally-incompatible element Nb forms a MORB-OIB array. However, enrichment of Th is relatively higher than Nb in a supra-subduction zone setting so that the associated rocks plot above the MORB-OIB array. Basic samples from Zone A plot subparallel to the MORB-OIB array with slightly higher Th/Yb ratios (Fig. 9b). These Th/Yb ratios, as well as Nb/Yb ratios, are positively correlated with their La/Yb ratios, indicating that the variation of these elements is affected by degrees of partial melting instead of fractional crystallization and/or crustal assimilation. These rocks are thus attributed to a dominant asthenospheric and/or Arabian lithospheric mantle source with a subordinate addition of continental crust or subduction-related components (Lustrino et al., 2010; Pearce et al., 1990; Shaw et al., 2003). The basic rocks from

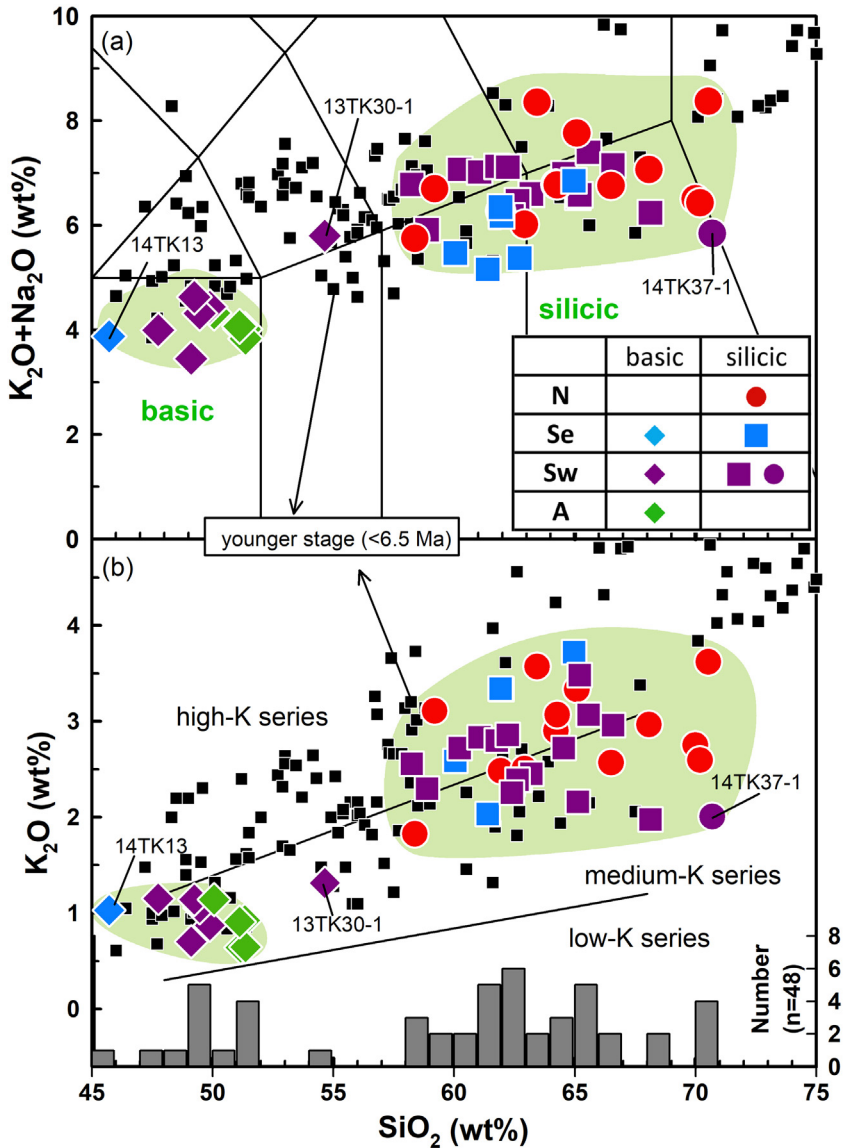


Fig. 6. Plots of (a) total alkalis versus silica (Le Maitre et al., 2005) and (b) SiO_2 versus K_2O (Peccerillo and Taylor, 1976). The sample abundance is shown by a histogram at the bottom. Symbols of samples: diamonds for basic rocks; squares and circles for silicic rocks with negative and positive ϵ_{Nd} values, respectively. For comparison, volcanic rocks of the younger stage (<6.5 Ma) are plotted as black squares (Lin et al., 2020; Pearce et al., 1990).

Zones Sw and Se both have lower Nb/Yb and higher Th/Yb ratios (Fig. 9a), which we ascribe to an enriched Tauride lithospheric mantle source, previously metasomatized during the Tethyan subduction-related processes (Dilek et al., 2010; Pearce et al., 1990). All of the silicic rocks plot well above the array except for rhyolite sample 14TK37-1 from Zone Sw (Fig. 9a). Although some silicic rocks can be derived from fractional crystallization of coeval basic rocks, the significantly higher Th/Yb and Nb/Yb ratios are interpreted as indicative of partial melts from the lower part of the continental crust that was heated from below by mantle-derived basaltic magmas.

6.3. Two crustal components in the magma genesis

The ϵ_{Nd} vs SiO_2 plot (Fig. 8) allows us to differentiate two types of crustal components in the CIA province that could be introduced through either crustal melting or minor crustal assimilation (AFC), in accord with the Pb—O isotopic variations in Keskin et al. (2006). The first crustal component is derived from a juvenile crust, such as the silicic rocks from Zone N, and rhyolite sample 14TK37-1, all with positive ϵ_{Nd} values. The second component is an older crust component, with

lower, negative ϵ_{Nd} values, such as the silicic rocks from Zones Sw and Se in the southern province. We note that a similar isotopic distinction is also recorded in earlier arc magmas from the respective geologic units, as illustrated by those of the late Cretaceous Elazig arc (Lin et al., 2019) from the Tauride block and the Paleogene Armenian arc (Lin et al., 2020) from the South Armenian block (Fig. 8).

It is beyond the scope of this paper to cast detailed discussion on how to form these two crustal components, which we relate simply to regional geologic history. The juvenile crust may have resulted mostly from recurrent underplating of basaltic magmas owing to complex subduction, accretion and collision processes that formed the Turkic-type orogen here (Şengör et al., 2008), and other accretionary orogens elsewhere (Cawood et al., 2009). Relative to this juvenile crust that prevails in the northern province, the older crust in the south is correlated to the Cadomian basements (Fig. 1a) and associated micro-continents or continental ribbons (Şengör, 1984). The presence of Cadomian rocks, which have negative present-day ϵ_{Nd} values of -5 to -10 (Beyarslan et al., 2016; Shafaii Moghadam et al., 2015; Ustaömer et al., 2009), supports the argument that the eastern Anatolian plateau is underlain by a continental basement (Topuz et al., 2017), rather than a young accretionary

Table 2

Whole-rock major and trace elements, and Sr—Nd isotopic data.

Area	A (basic)				Sw (basic)				Sw (silicic)												Adamkiran							
	Yavuzeli				Inle				Adamkiran				Yamadag				Inle											
Sample no.	13TK71	13TK72-1	13TK72-2	13TK73	13TK74	14TK45	14TK68	13TK30-1	14TK34	14TK36	14TK38	13TK05	14TK46	14TK47	14TK48	14TK49	14TK50	14TK51	14TK52	14TK53	14TK54	14TK63	14TK65-1	14TK66				
Latitude (N)	37.4104	37.3986	37.3986	37.3576	37.2671	39.0118	38.7181	39.0316	39.0137	39.0137	39.1948	38.8407	38.9826	38.9826	38.9921	38.9921	38.9921	39.0351	39.0351	39.0351	38.9641	38.3458	38.3454	38.3577				
Longitude (E)	37.6176	37.5727	37.5727	37.5425	37.5481	38.9334	37.3096	38.4732	38.4856	38.4856	38.2110	39.2519	38.9969	38.9969	39.0439	39.0439	39.0439	39.0465	39.0465	39.0465	39.1976	37.6716	37.6551	37.6119				
Age (Ma)	16.9 ± 0.4				10.4 ± 0.2				15.8 ± 0.2				10.7 ± 0.2				15.4 ± 0.2				15.0 ± 0.2				15.7 ± 0.2		16.3 ± 0.2*	
Major element (wt%)																												
SiO ₂	51.17	51.34	50.07	51.37	51.12	47.76	49.11	54.65	49.90	49.47	49.25	64.54	65.57	60.23	63.20	66.58	65.13	61.05	61.78	62.23	58.25	62.62	62.39	65.20				
TiO ₂	1.37	1.58	1.86	1.70	1.76	1.89	1.54	1.62	1.34	1.70	2.01	0.59	0.55	0.83	0.62	0.38	0.42	0.70	0.69	0.69	0.92	0.72	0.81	0.62				
Al ₂ O ₃	13.96	14.19	13.86	14.88	14.10	14.21	14.91	18.25	16.53	15.78	14.87	17.45	16.12	16.94	17.21	15.96	17.53	16.16	16.45	16.41	16.83	16.17	16.15	15.68				
tFe ₂ O ₃	10.81	12.01	12.07	11.82	11.58	11.56	12.25	8.30	9.86	10.10	11.67	3.10	3.39	4.91	3.94	2.37	2.77	4.29	4.28	4.29	5.44	4.34	4.82	3.77				
MnO	0.14	0.15	0.14	0.11	0.14	0.15	0.14	0.11	0.15	0.14	0.14	0.04	0.04	0.04	0.06	0.02	0.05	0.07	0.07	0.07	0.06	0.03	0.06	0.05				
MgO	6.58	7.69	6.81	5.57	7.35	9.65	8.68	2.58	6.98	6.71	7.52	1.08	1.65	1.26	1.96	0.55	1.55	2.68	2.72	2.71	2.97	1.67	2.84	2.43				
CaO	9.61	7.99	8.82	7.86	8.28	9.22	8.56	6.90	8.49	9.26	8.52	3.57	3.63	4.55	4.33	3.26	3.75	4.73	4.71	4.62	5.94	4.50	4.95	3.64				
Na ₂ O	3.38	3.09	3.18	3.19	3.16	2.85	2.75	4.49	3.57	3.26	3.49	4.26	4.33	4.35	4.15	4.20	4.38	4.19	4.33	4.26	4.23	4.08	3.93	3.10				
K ₂ O	0.64	0.92	1.14	0.65	0.91	1.15	0.70	1.31	0.87	1.06	1.14	2.72	3.07	2.72	2.45	2.96	2.16	2.83	2.80	2.86	2.56	2.39	2.26	3.49				
P ₂ O ₅	0.16	0.22	0.28	0.20	0.23	0.26	0.21	0.30	0.23	0.38	0.34	0.24	0.19	0.25	0.19	0.13	0.11	0.33	0.34	0.41	0.17	0.17	0.16					
LOI	2.11	0.53	1.45	1.88	0.86	1.03	1.32	0.90	1.89	1.44	0.20	1.52	0.61	1.27	1.72	1.57	1.41	1.18	1.08	1.42	1.87	2.13	1.25	1.91				
Total	99.93	99.70	99.69	99.22	99.50	99.72	100.17	99.41	99.81	99.29	99.15	99.10	99.14	97.35	99.83	97.97	99.27	98.21	99.23	99.89	99.47	98.84	99.62	100.05				
Trace element (ppm)																												
Sc	26.9	16.0	26.5	30.5	28.4	10.6	15.8	16.1	18.2	15.3	10.1	16.9	1.7	6.3	2.8	1.0	1.2	2.9	4.1	2.8	11.8	7.6	7.1	6.7				
V	141	157	156	150	155	189	153	153	156	195	193	37.8	55.1	79.3	65.3	49.0	34.5	75.6	69.4	79.2	99.6	69.5	86.5	55.4				
Cr	246	277	255	234	232	340	314	22	144	307	301	12	36	32	18	46	61	48	48	41	111	46	83	94				
Co	44.5	46.9	48.4	34.7	47.5	49.2	50.5	20.7	37.0	38.4	43.0	6.0	8.4	11.9	7.9	6.7	7.8	12.2	11.6	12.1	15.7	7.6	13.8	10.8				
Ni	242	226	213	184	220	175	203	21.0	85.8	176	158	8.60	22.9	23.6	11.2	25.5	31.5	29.5	27.0	27.0	75.1	22.6	43.2	41.9				
Cu	62.9	69.3	70.7	79.2	70.8	47.2	59.4	40.0	38.1	58.2	58.8	8.17	11.3	19.5	8.71	28.5	72.0	24.7	34.7	17.7	13.3	23.7	26.1	15.7				
Zn	117	95.7	108	144	87.6	96.8	129	79.8	67.2	72.2	118	54.8	35.2	203	102	61.8	56.1	128	134	54.1	67.9	–	–	47.3				
Ga	20.5	20.7	21.2	21.0	20.6	21.0	20.2	19.6	18.0	19.2	22.5	19.9	20.4	22.0	21.7	22.0	28.0	22.5	23.1	21.6	22.0	19.1	18.6	18.8				
Rb	17.7	30.6	24.3	7.94	27.1	29.4	15.4	35.6	28.2	23.9	19.4	107	141	111	127	139	40.2	115	108	113	94.7	109	74.1	86.0				
Sr	267	263	324	276	305	393	307	398	313	463	472	415	471	515	465	351	391	653	626	637	749	283	264	253				
Y	19.6	21.5	21.8	21.8	21.6	19.5	18.6	25.7	24.0	27.4	21.1	9.6	12.6	17.7	15.8	12.7	9.6	16.5	16.3	17.1	16.8	14.1	14.2	14.2				
Zr	78.0	105	133	104	114	131	100	172	141	178	154	165	180	218	162	154	166	216	208	219	215	152	153	173				
Nb	8.2	11.8	18.7	12.3	15.8	14.7	10.0	12.0	7.8	19.3	17.9	9.8	15.7	17.7	10.9	10.5	10.5	27.4	26.1	27.7	31.1	8.3	8.2	8.8				
Cs	0.71	1.16	0.74	0.21	0.79	1.24	2.34	1.18	2.47	0.91	0.36	4.99	12.2	5.03	8.50	8.70	0.46	6.22	6.34	6.52	4.28	5.99	4.80	8.06				
Ba	680	157	244	156	172	167	131	199	142	274	249	501	650	594	578	498	555	759	723	748	698	323	293	344				
La	7.20	11.2	15.8	10.9	12.4	12.6	11.1	18.0	13.9	29.7	16.2	26.6	36.2	38.5	30.0	32.5	26.5	46.3	45.9	50.2	52.4	21.6	18.2	21.5				
Ce	15.7	23.8	32.9	20.4	26.8	27.3	24.0	35.3	29.0	50.9	32.4	49.6	62.3	66.3	54.6	48.4	44.6	81.7	80.5	87.8	91.8	41.0	38.9	43.8				
Pr	2.06	3.14	4.03	2.99	3.31	3.46	3.02	4.22	3.38	6.49	4.21	5.45	6.30	7.19	5.90	6.31	4.95	8.50	8.37	8.99	9.54	4.62	4.24	4.79				
Nd	9.47	13.1	17.6	13.3	14.6	15.1	13.4	17.6	14.5	26.9	18.6	20.5	21.7	25.8	21.8	22.7	17.6	29.7	29.4	31.2	33.6	17.5	16.5	18.2				
Sm	2.80	3.55	4.38	3.65	3.84	3.74	3.38	4.13	3.44	5.54	4.40	3.83	3.60	4.64	3.98	3.97	3.10	4.89	4.79	5.04	5.43	3.48	3.39	3.59				
Eu	1.08	1.22	1.45	1.30	1.31	1.29	1.16	1.36	1.14	1.68	1.49	1.03	0.95	1.23	1.02	0.93	0.84	1.27	1.22	1.28	1.42	0.93	0.92	0.91				
Gd	3.49	3.98	4.70	4.23	4.30	4.01	3.77	4.47	3.89	5.49	4.64	2.86	2.77	3.70	3.26	3.06	2.32	3.68	3.63	3.81	4.09	3.07	3.21	3.08				
Tb	0.58	0.66	0.74	0.69	0.68	0.62	0.59	0.72	0.65	0.83	0.71	0.40	0.40	0.56	0.49	0.44	0.34	0.53	0.53	0.55	0.58	0.46	0.48	0.46				
Dy	3.51	3.94	4.18	4.08	4.04	3.62	3.51	4.42	3.98	4.75	4.01	1.98	2.16	3.10	2.72	2.28	1.76	2.87	2.85	2.98	3.02	2.58	2.92	2.68				
Ho	0.70	0.78	0.79	0.77	0.76	0.69	0.67	0.92	0.84	0.94	0.74	0.34	0.41	0.60	0.52	0.42	0.33	0.55	0.54	0.57	0.49	0.56	0.51					
Er	1.85	1.98	2.05	2.08	2.04	1.82	1.85	2.63	2.43	2.58	1.95	0.83	1.18	1.69	1.45	1.13	0.89	1.52	1.51	1.57	1.54	1.38	1.58	1.47				
Tm	0.25	0.27	0.27	0.28	0.28	0.25	0.25	0.39	0.37	0.36	0.27	0.11	0.18	0.25	0.21	0.16	0.12	0.23	0.22	0.24	0.21	0.20	0.23	0.21				
Yb	1.53	1.68	1.60</																									

Area	Se (basic)								Se (silicic)																
	Yamadag				Aladag				Erzurum				Uzundere				Kars		Goderdzi						
Sample no.	14TK67	14TK41	14TK37-1	14TK13	14TK14	14TK15	14TK16	14TK17-3	14TK18	14TK20	15TK49	15TK51	15TK52	15TK54	15TK55	15TK56	15TK57	15TK83	13GE04-5	13GE05-2	13GE06	13GE07	13GE08	13GE09-2	
Latitude (N)	38.7201	39.2231	39.0326	39.1528	39.1442	39.1344	39.3602	39.3602	39.3602	40.0884	40.1412	40.1349	40.1571	40.1571	40.5139	40.5070	41.1837	41.4790	41.3784	41.3811	41.3810	41.3577	41.3625		
Longitude (E)	37.3482	38.2704	38.3270	43.5855	43.5707	43.5518	43.5419	43.5419	43.5419	41.4282	41.3962	41.3749	41.3643	41.3643	41.5251	41.5145	42.5836	43.2851	43.2832	43.2822	43.2870	43.2529	43.2796		
Age (Ma)	9.0 ± 0.2	11.6 ± 0.2		14.8 ± 0.2	14.3 ± 0.2	17.2 ± 0.2		17.2 ± 0.2			5.6 ± 0.3	6.0 ± 0.3	8.5 ± 0.3	8.2 ± 0.3	8.0 ± 0.3	7.6 ± 0.5	7.4 ± 0.3	7.5 ± 0.2			7.5 ± 0.3				
Major element (wt%)																									
SiO ₂	58.88	68.13	70.69	45.72	62.72	60.05	61.96	61.92	64.96	61.39	58.38	59.87	64.27	61.93	62.91	69.99	70.18	66.50	65.08	70.53	64.22	59.19	63.43	68.07	
TiO ₂	0.88	0.34	0.23	1.51	0.61	0.70	0.69	0.73	0.61	0.62	0.88	0.83	0.60	0.82	0.70	0.29	0.28	0.53	0.56	0.29	0.46	0.82	0.72	0.41	
Al ₂ O ₃	17.28	15.87	15.30	13.98	16.97	15.96	16.08	16.03	16.08	15.97	16.82	16.77	15.88	16.40	16.92	15.95	15.90	16.20	16.24	15.30	16.48	16.04	16.26	15.91	
tFe ₂ O ₃	6.21	2.25	1.64	10.20	4.74	6.24	5.28	5.86	4.92	4.39	5.49	5.62	3.88	4.95	4.46	1.45	1.49	3.29	3.00	1.47	2.87	5.13	3.93	2.48	
MnO	0.12	0.05	0.05	0.15	0.05	0.09	0.06	0.06	0.04	0.08	0.09	0.08	0.06	0.05	0.07	0.02	0.03	0.06	0.04	0.04	0.02	0.08	0.12	0.04	
MgO	3.85	0.84	0.57	9.97	1.73	2.83	2.34	1.85	1.14	1.90	3.54	2.47	2.27	1.82	2.46	0.48	0.82	1.46	1.18	0.42	0.85	3.10	1.10	0.66	
CaO	5.83	3.21	2.97	13.72	4.04	5.79	4.01	4.18	3.55	4.62	6.91	6.36	4.52	4.54	3.82	2.67	3.21	3.61	3.40	1.75	3.26	5.20	3.19	3.22	
Na ₂ O	3.61	4.26	3.84	2.85	2.99	2.88	2.85	3.01	3.13	3.13	3.92	4.19	3.70	3.79	3.51	3.75	3.83	4.19	4.43	4.75	3.88	3.59	4.78	4.10	
K ₂ O	2.30	1.98	2.01	1.03	2.39	2.59	3.33	3.34	3.72	2.03	1.83	2.02	3.07	2.48	2.50	2.75	2.60	2.57	3.33	3.62	2.90	3.11	3.57	2.97	
P ₂ O ₅	0.32	0.15	0.10	0.43	0.17	0.15	0.19	0.20	0.16	0.16	0.30	0.28	0.24	0.28	0.25	0.09	0.09	0.16	0.32	0.12	0.20	0.39	0.32	0.17	
LOI	0.48	1.82	1.33	0.53	2.35	1.84	4.00	1.35	1.48	3.38	1.08	0.81	1.48	1.48	2.22	1.25	1.63	1.35	2.08	1.34	3.88	2.50	0.96	1.49	
Total	99.76	98.88	98.70	100.08	98.75	99.14	100.78	98.52	99.81	97.67	99.22	99.30	99.97	98.53	99.82	98.69	100.05	99.92	99.65	99.62	99.00	99.13	98.39	99.50	
Trace element (ppm)																									
Sc	9.6	–	6.7	24.8	22.5	21.1	7.0	7.4	14.4	5.5	21.3	20.0	15.9	21.6	17.7	8.8	14.7	4.0	12.6	–	13.8	6.0	4.4	19.4	
V	98.2	23.2	15.1	195	111	145	111	180	148	89.8	103	92	65.5	67.0	46.5	21.9	22.6	35.1	57.7	17.7	44.4	98.4	58.7	42.9	
Cr	58	9	12	263	43	57	14	10	13	91	65	93	43	80	18	58	51	29	13	23	63	7.0	13		
Co	18.7	3.7	2.9	45.3	11.1	16.2	10.8	11.1	8.6	8.7	18.4	17.0	11.1	12.0	13.6	3.6	4.4	8.6	7.0	2.7	6.0	15.1	9.5	5.4	
Ni	40.6	5.01	7.05	193	22.1	23.8	5.90	4.75	5.58	4.36	57.9	46.6	46.3	31.0	59.6	8.3	32.0	21.2	22.7	9.25	16.5	50.7	10.8	9.67	
Cu	19.7	16.5	13.2	105	14.2	33.0	15.8	7.2	15.2	15.8	34.2	23.8	32.8	26.0	29.3	12.8	12.1	28.4	15.5	6.95	31.4	12.5	13.2	26.0	
Zn	39.8	43.7	37.0	74.7	116	63.5	83.1	58.0	53.6	80.9	65.6	69.1	119	66.6	68.7	46.4	45.9	49.4	89.5	39.1	38.4	69.7	63.2	109	
Ga	19.5	18.6	15.2	16.7	17.9	17.8	19.4	19.2	19.7	20.4	14.3	15.7	19.0	14.4	16.1	20.3	17.8	24.2	17.9	17.6	18.5	18.2	18.5	18.6	
Rb	38.5	64.0	61.7	24.1	89.2	93.3	124	129	154	152	38.9	52.0	70.6	68.3	58.0	111	107	71.6	93.0	122	91.4	73.4	97.6	109	
Sr	342	299	263	718	345	443	391	508	328	345	621	504	431	442	346	352	382	381	665	382	653	759	666	545	
Y	21.7	11.0	6.9	21.4	35.5	29.7	22.5	22.4	23.0	23.8	16.5	15.5	11.4	15.0	13.9	4.2	4.3	12.3	11.5	10.8	9.4	16.6	17.4	6.0	
Zr	209	203	122	118	157	136	185	187	178	179	148	165	168	176	181	105	105	159	204	165	168	191	254	147	
Nb	22.4	10.4	8.8	13.5	14.3	13.0	25.3	25.0	26.4	19.1	12.2	11.6	11.0	14.6	12.6	4.9	4.8	13.1	15.6	20.0	14.2	16.1	20.2	9.8	
Cs	3.87	1.52	2.13	1.22	4.62	3.82	8.04	4.45	5.47	8.97	1.27	1.39	3.50	1.57	0.97	6.32	6.58	1.93	2.85	4.48	3.86	2.26	1.56	4.13	
Ba	470	436	615	387	639	602	798	850	659	687	425	413	491	510	531	487	473	574	918	817	738	755	1028	837	
La	32.6	26.6	12.6	32.1	33.0	33.8	46.2	65.8	31.4	38.3	30.2	29.5	31.1	42.1	36.5	21.4	19.3	22.2	37.8	35.1	34.7	39.7	44.3	32.5	
Ce	62.4	47.5	31.2	62.8	60.9	51.0	83.6	104	61.7	70.9	52.6	52.3	53.6	60.4	56.4	33.8	30.7	38.8	66.2	61.0	57.9	71.1	81.0	53.3	
Pr	6.43	4.95	2.68	7.20	6.72	6.34	8.93	11.4	6.92	7.52	5.81	5.57	5.46	7.71	6.62	3.18	2.91	4.15	6.91	6.17	5.90	7.76	8.59	5.38	
Nd	24.0	17.3	9.83	28.4	26.5	24.1	32.0	39.2	25.9	27.2	21.7	20.1	19.1	27.0	23.0	10.4	9.51	14.5	23.1	19.0	19.1	26.9	29.1	17.7	
Sm	4.62	2.95	1.76	5.20	5.33	4.58	5.67	6.37	4.82	5.02	3.97	3.64	3.24	4.54	3.96	1.67	1.56	2.62	3.53	2.93	2.87	4.50	4.64	2.71	
Eu	1.23	0.83	0.52	1.59	1.50	1.16	1.36	1.49	1.14	1.16	1.17	1.09	0.90	1.20	0.96	0.53	0.52	0.80	0.99	0.71	0.83	1.21	1.24	0.78	
Gd	4.29	2.35	1.54	4.67	5.95	4.54	4.46	4.99	4.08	4.40	3.49	3.20	2.88	3.66	3.22	1.21	1.14	2.27	3.05	2.56	2.39	3.96	3.95	2.26	
Tb	0.68	0.35	0.24	0.70	0.94	0.71	0.69	0.74	0.63	0.69	0.51	0.48	0.37	0.53	0.46	0.16	0.16	0.35	0.35	0.31	0.29	0.50	0.52	0.24	
Dy	4.04	1.85	1.38	4.01	5.70	4.27	3.90	4.06	3.67	3.98	2.92	2.73	2.01	2.84	2.52	0.78	0.77	2.04	2.00	1.77	1.55	2.80	2.95	1.11	
Ho	0.80	0.34	0.27	0.75	1.19	0.90	0.78	0.79	0.74	0.80	0.56	0.54	0.38	0.53	0.47	0.13	0.14	0.40	0.39	0.36	0.31	0.58	0.61	0.20	
Er	2.33	0.96	0.73	2.10	3.40	2.65	2.26	2.23	2.16	2.32	1.59	1.49	1.05	1.41	1.31	0.37	0.36	1.19	1.09	0.99	0.87	1.57	1.69	0.52	
Tm	0.35	0.14	0.12	0.29	0.52	0.40	0.35	0.34	0.34	0.35	0.23	0.22	0.15	0.20	0.19	0.05	0.05	0.18	0.16	0.15	0.13	0.23	0.26	0.07	
Yb	2.22	0.89	0.75	1.78	3.29	2.49	2.29	2.18	2.24	2.27	1.41	1.40	0.96	1.22	1.19	0.33	0.34	1.							

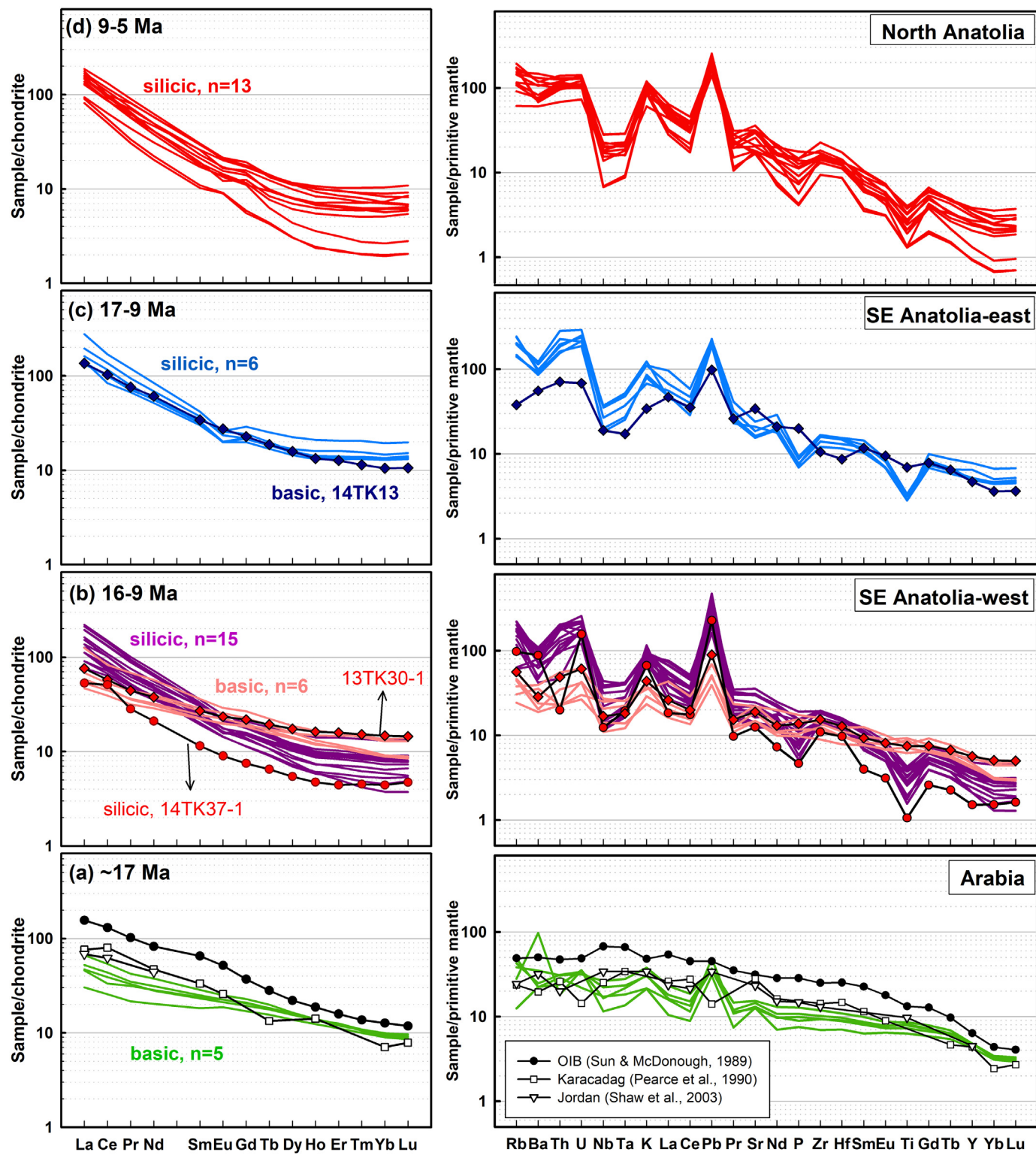


Fig. 7. REE and primitive mantle normalized incompatible element diagrams. OIB-type basaltic rocks from Karacadag (Pearce et al., 1990) and Jordan (Shaw et al., 2003) in the Arabian foreland are plotted for comparison. The OIB and normalizing values are from Sun and McDonough (1989).

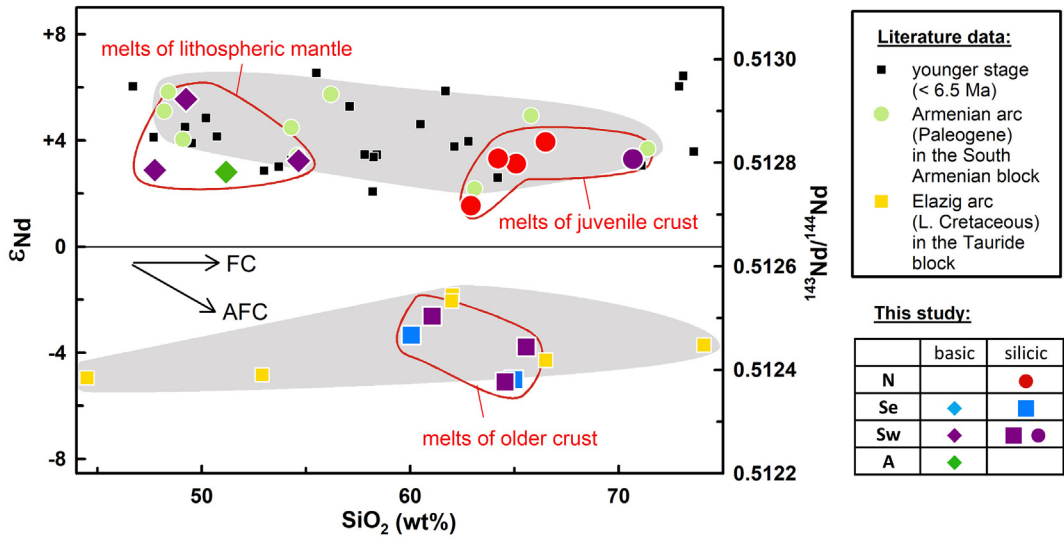


Fig. 8. Correlation diagram of Nd isotopic ratios and SiO_2 contents. The arrows show the fractional crystallization trends with or without crustal assimilation (AFC or FC). Data sources for samples of the younger stage are the same as Fig. 6. Data of the Armenian arc and the Elazig arc (final stage only) are from Lin et al. (2020) and Lin et al. (2019), respectively.

complex (Keskin, 2003; Sengör et al., 2008). This argument is further supported by our inherited zircon data described above, and available detrital zircon ages (cf. Topuz et al., 2017), both pointing to Neoproterozoic to early Paleozoic crustal sources.

6.4. Migrating magmatism in the CIA province and beyond

In Fig. 10, we depict the post-collisional magmatic migration that is observed both in the initial stage and a subsequent, younger stage, within and beyond the CIA province. Note that, in contrast to the bimodal volcanic suite in the initial stage, a broad spectrum of calc-alkaline and subordinate alkaline rocks from mafic to felsic lithologies occur in the younger stage (see the age and geochemical dataset compiled in supplementary material #4). Below we give a summary of the magmatic evolution:

6.4.1. Initiation stage I (southern province)

The bimodal eruptions started at ~17 Ma in the Arabian foreland (Zone A) and the Yamadag and Van fields (Zones Sw and Se, respectively), SE Anatolia (Fig. 10a). These were followed by small eruptions at ~11 Ma, forming the Kotek basalts and Kosedag dacites around the Erzurican-Kars Suture and ultrapotassic rocks in Saray, NW Iran. This stage of initial volcanism, lasting until ~9 Ma, was confined to the southern province.

6.4.2. Initiation stage II (northern province)

The initial volcanism then migrated northward to form the Erzurum and Kars fields (Zone N) in NE Anatolia. This stage was active during ~9–5 Ma and was dominated by silicic eruptions (Fig. 10b). Nevertheless, as mentioned above, subordinate amounts of basic eruptions did occur in the northern province.

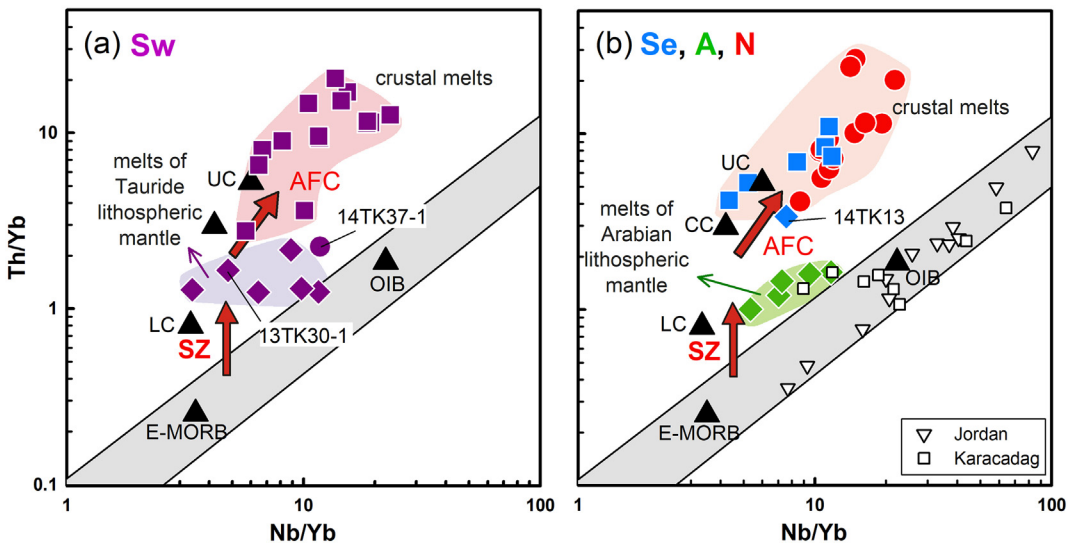


Fig. 9. Correlation diagram of Nb/Yb versus Th/Yb (Pearce, 2008). The red arrows highlight the crustal input through the subduction zone (SZ) process or AFC in causing a shift to compositions above the MORB-OIB array. Symbols are the same as Fig. 6. The average E-MORB and OIB values are from Sun and McDonough (1989); The average lower crust (LC), upper crust (UC) and total continental crust (CC) are from Rudnick and Gao (2014). The OIB-type basalts of Jordan and Karacadag are from Shaw et al. (2003) and Lustrino et al. (2010). (For interpretation of the references to colour in this figure legend, the reader is referred to the web version of this article.)

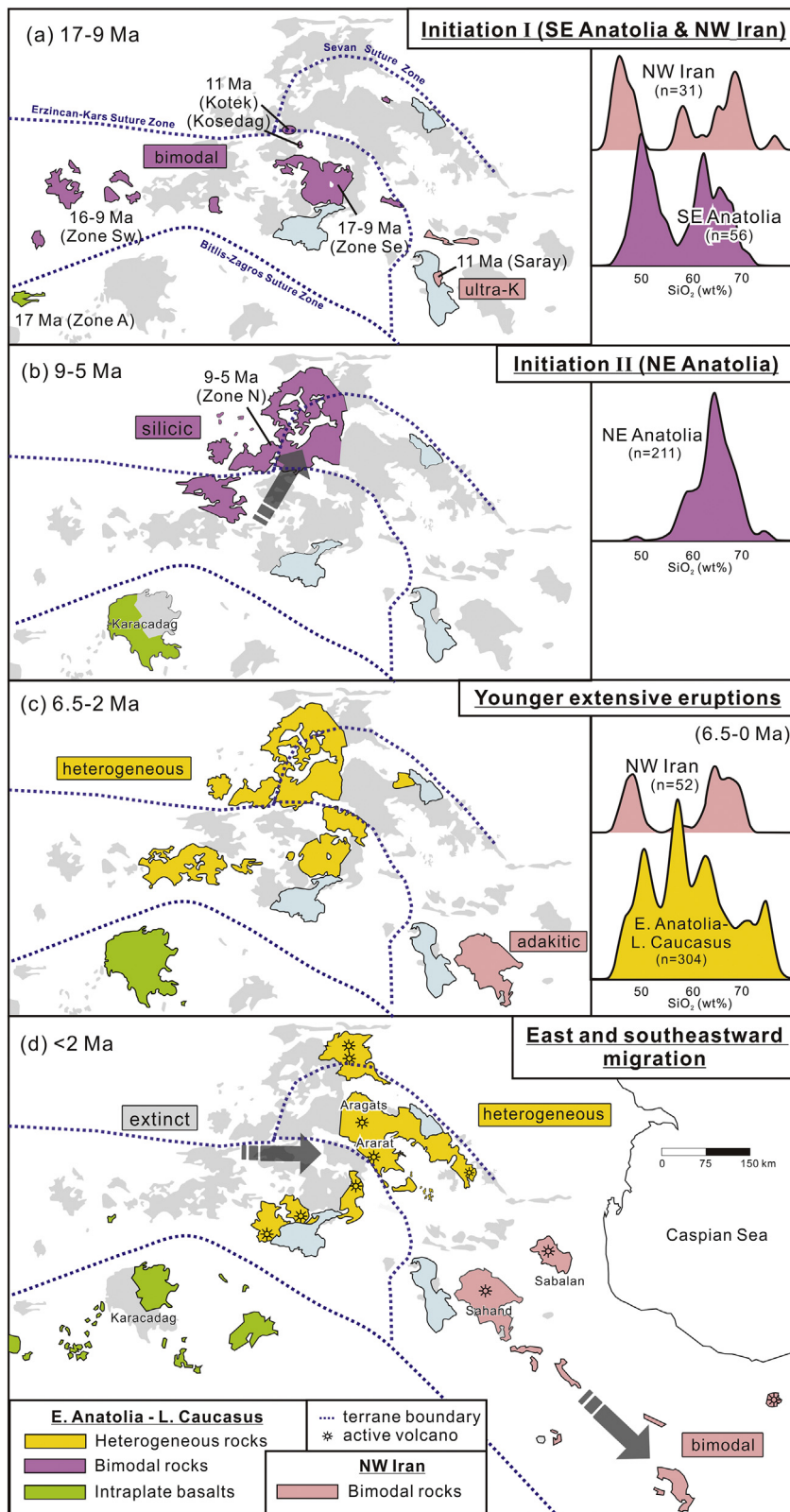


Fig. 10. (a)–(d) Time-slice maps showing the distribution and magma types of the post-collisional volcanism in and around the CIA province. Histograms of sample abundance as a function of silica contents are shown on the right-hand side. Active volcanic fields are filled in colors, while those in gray are either inactive or of age-unknown.

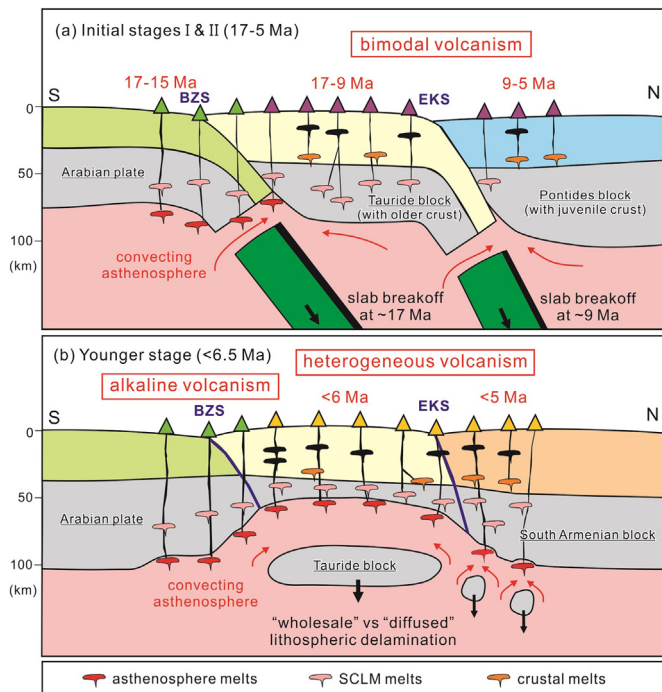


Fig. 11. Lithospheric cross-sections showing the CIA magmatic evolution: (a) the initial stage from Karacadag to Kars in the west, and (b) the younger stage from Karacadag to Lesser Caucasus in the east, considering the eastward migration since ~2 Ma.

6.4.3. A younger and extensive stage

From ~6.5 Ma, the volcanism became more extensive and formed widespread volcanic rocks in the CIA province, including the main basaltic flows from Mt. Karacadag and adakitic ignimbrites from Mt. Sahand, NW Iran (Fig. 10c). Whereas eruptions in the northern province appear to be a continuation of initial stage II, characterized by bimodal volcanism with dominantly of basaltic lavas (Keskin et al., 2006), those in the southern province occurred as a renewal phase after a magmatic gap of ~3 m.y. (Fig. 5). This renewal is characterized by compositional heterogeneities (Figs. 6), and by positive ϵ_{Nd} values in all rock types (Fig. 8). We attribute this dramatic change, which occurred within ~3 my, to “wholesale” delamination of the thickened lithospheric mantle (see next section).

6.4.4. East- and southeastward migration

Subsequent volcanic migration took place at ~2 Ma (Fig. 10d), marked by an eastward migration of erupting centers first reported by Innocenti et al. (1976). At this time, the volcanic activity in the west became extinct. Meanwhile, bimodal magmatism started in NW Iran (Fig. 10d), forming a suite of basaltic and adakitic rocks in and south of two gigantic volcanoes Mts. Sahand and Sabalan (Lechmann et al., 2018; Pang, KN et al., unpubl. data). This nascent volcanic activity then propagated southeastward along the Urumieh-Dokhtar magmatic belt (Fig. 1b), to the Quaternary (~0.1 Ma) high-Mg ultrapotassic volcanic rocks found in SE Iran (Pang et al., 2015). The propagating onset of post-collisional magmatism in the region is consistent with the notion of an oblique continental collision between Arabia and Eurasia.

6.5. Geodynamic and broader implications

The post-collisional magmatic evolution in the CIA province is controlled mainly by two major geodynamic processes (Fig. 11). To account for the northward initiation of bimodal magmatism (~17–5 Ma), we adopt the “double slab breakoff” model by Skobeltsyn et al. (2014) and

argue that two successive breakoff events took place at ~17 Ma in the south and ~9 Ma in the north (Fig. 11a). Such slab detachments would allow the hotter convective asthenosphere to rise and partially melt (Van de Zedde and Wortel, 2001), and cause further melting in the overlying lithospheric mantle, giving rise to the basic magmas in the peri-Arabia zone. The basic magmas, in turn, would have partially underplated, and heated the lower part of the continental crust, thus forming crustal melts. We note that an early slab breakoff at ~17 Ma along the Bitlis-Zagros Suture is supported by apatite fission-track age data that suggest rapid exhumation in the Bitlis thrust zone between 18 and 13 Ma (Okay et al., 2010; see Fig. 5). Although no direct uplift evidence exists to constrain the late slab breakoff, the occurrence of late Miocene-early Pliocene erosion surface in Eastern Anatolia (Erinç, 1953) and the increase in exhumation rate in the Lesser Caucasus from ~5 Ma (Chen et al., 2013) are consistent with multi-phased uplift in the CIA province and a later uplift in the north at that time.

In the younger stage (<6.5 Ma), the more extensive and heterogeneous volcanism is best explained by “wholesale” lithospheric delamination in the southern province, i.e., removal of the lower part of the thickened Tauride block (Fig. 11b). This root removal would intensify mantle and crustal melting (Pearce et al. (1990)), and also enhance the extensional stress that led to regional lithospheric thinning. Consequently, in contrast to the occurrence of adakitic rocks (i.e., those with low HREE from Zones Sw and N; Fig. 7) observed in the initial stage and illustrative of melting and/or the presence of a thick crust; younger stage adakitic rocks are absent (see supplementary material #4) and thus indicate decreasing crustal thickness. This argument is consistent with the current Moho depth of 34–46 km associated with a relatively thinner lithosphere in the southern province, estimated from seismic tomographic results (Angus et al., 2006; Tezel et al., 2013). A smaller scale, or “diffused” mode of delamination of a relatively thicker lithosphere (Fig. 11b) may have been operating beneath the northern province, i.e., the South Armenian block as suggested by Neill et al. (2015), accounting for the younger stage of magmatism in the northern province.

Supplementary data to this article can be found online at <https://doi.org/10.1016/j.lithos.2020.105394>.

Declaration of Competing Interest

None.

Acknowledgments

We thank Chien-Hui Hung, Jia-Huei Chen and Chun Lin for laboratory assistance; Mehmet Ali Erturk, Mustafa Eren Rizeli and Abdullah Sar for their assistance help in the field; George S. Burr for language editing. Comments by Julian A. Pearce, an anonymous reviewer and the Edior Xian-Hua Li helped improve the presentation of the paper. This study was performed under a joint research program between Firat University, National Taiwan University and Academia Sinica, and financially supported by the Ministry of Science and Technology, Republic of China (Taiwan) under the grant MOST108-2639-M-001-002-ASP.

References

- Adamia, S., Alania, V., Chabukiani, A., Chichua, G., Enukidze, O., Sadradze, N., 2010. Evolution of the late Cenozoic basins of Georgia (SW Caucasus): a review. *Geol. Soc. Lond. Spec. Publ.* 340, 239–259.
- Aghanabati, A., 1993. Geological map of the Middle East 1:5000000. Commission for the Geological Map of the World. Sub-Commission for the Middle East, 2nd Ed Geological Survey of Iran Commission.
- Allen, M.B., Armstrong, H.A., 2008. Arabia–Eurasia collision and the forcing of mid-Cenozoic global cooling. *Palaeogeogr. Palaeoclimatol. Palaeoecol.* 265, 52–58.
- Angus, D., Wilson, D.C., Sandvol, E., Ni, J., 2006. Lithospheric structure of the Arabian and Eurasian collision zone in eastern Turkey from S-wave receiver functions. *Geophys. J. Int.* 166, 1335–1346.
- Arger, J., Mitchell, J., Westaway, R.W., 2000. Neogene and Quaternary volcanism of southeastern Turkey. *Geol. Soc. Lond. Spec. Publ.* 173, 459–487.

- Beyarslan, M., Lin, Y.-C., Bingöl, A.F., Chung, S.-L., 2016. Zircon U-Pb age and geochemical constraints on the origin and tectonic implication of Cadomian (Ediacaran–early Cambrian) magmatism in SE Turkey. *J. Asian Earth Sci.* 130, 223–238.
- Castillo, P.R., 2012. Adakite petrogenesis. *Lithos* 134, 304–316.
- Cawood, P.A., Kröner, A., Collins, W.J., Kusky, T.M., Mooney, W.D., Windley, B.F., 2009. In: Cawood, P.A., Kröner, A. (Eds.), *Accretionary orogens through earth history*. 318. Geological Society, London, pp. 1–36 Special Publication.
- Chen, C.-T., Lee, Y.-H., Chung, S.-L., Galoyan, G., Melkonyan, R., Karakhanian, A., 2013. Exhumation of the Less Caucasus and its Implication to Uplift of Eastern Anatolia Plateau, 2013 Fall Meeting. AGU.
- Chiu, H.-Y., Chung, S.-L., Zarrinkoub, M.H., Mohammadi, S.S., Khatib, M.M., Iizuka, Y., 2013. Zircon U-Pb age constraints from Iran on the magmatic evolution related to Neotethyan subduction and Zagros orogeny. *Lithos* 162, 70–87.
- Chung, S.L., Chu, M.F., Zhang, Y., Xie, Y., Lo, C.H., Lee, T.Y., Lan, C.Y., Li, X., Zhang, Q., Wang, Y., 2005. Tibetan tectonic evolution inferred from spatial and temporal variations in post-collisional magmatism. *Earth Sci. Rev.* 68, 173–196.
- Dilek, Y., Imanverdiyev, N., Altunkaynak, Ş., 2010. Geochemistry and tectonics of Cenozoic volcanism in the Lesser Caucasus (Azerbaijan) and the peri-Arabian region: collision-induced mantle dynamics and its magmatic fingerprint. *Int. Geol. Rev.* 52, 536–578.
- Ercan, T., Fujitami, T., Madsuda, J.-I., Notsu, K., Uti, T., 1990. *Doğu ve Güneydoğu Anadolu Neojen-Kuvaterner volkanitlerine ilişkin yeni jeokimyasal, radyometrik ve izotopik verilerin yorumu. Maden Tektik ve Arama Dergisi* 110.
- Erinç, S., 1953. *Doğu Anadolu Coğrafyası. İstanbul Üniv. Yayınları* No. 572, 124.
- Innocenti, F., Mazzuoli, R., Pasquare, G., Radicati di Brozolo, F.R., Villari, L., 1976. Evolution of the volcanism in the area of interaction between the Arabian, Anatolian and Iranian plates (lake Van, eastern Turkey). *J. Volcanol. Geotherm. Res.* 1, 103–112.
- Innocenti, F., Mazzuoli, R., Pasquare, G., Radicati di Brozolo, F., Villari, L., 1982. Tertiary and Quaternary volcanism of the Erzurum-kars area (Eastern Turkey): geochronological data and geodynamic evolution. *J. Volcanol. Geotherm. Res.* 13, 223–240.
- Jolivet, L., Faccenna, C., 2000. Mediterranean extension and the Africa-Eurasia collision. *Tectonics* 19, 1095–1106.
- Keskin, M., 2003. Magma generation by slab steepening and breakoff beneath a subduction-accretion complex: an alternative model for collision-related volcanism in Eastern Anatolia, Turkey. *Geophys. Res. Lett.* 30, 8046.
- Keskin, M., Pearce, J.A., Mitchell, J., 1998. Volcano-stratigraphy and geochemistry of collision-related volcanism on the Erzurum-Kars Plateau, northeastern Turkey. *J. Volcanol. Geotherm. Res.* 85, 355–404.
- Keskin, M., Pearce, J.A., Kempton, P.D., Greenwood, P., 2006. Magma-crust interactions and magma plumbing in a postcollisional setting: geochemical evidence from the Erzurum-Kars volcanic plateau, eastern Turkey. *Spec. Pap. Geol. Soc. Am.* 409, 475.
- Kürüm, S., Önal, A., Boztuğ, D., Spell, T., Arslan, M., 2008. 40 Ar/39 Ar age and geochemistry of the post-collisional Miocene Yamadağ volcanics in the Arapkir area (Malatya province), eastern Anatolia, Turkey. *J. Asian Earth Sci.* 33, 229–251.
- Le Maitre, R.W., Streckeisen, A., Zanettin, B., Le Bas, M., Bonin, B., Bateman, P., 2005. *Igneous Rocks: A Classification and Glossary of Terms*. Recommendations of the International Union of Geological Sciences Subcommission on the Systematics of Igneous Rocks. 2nd ed. Cambridge University Press, New York.
- Lebedev, V.A., Sharkov, E.V., Keskin, M., Oyan, V., 2010. Geochronology of late Cenozoic volcanism in the area of Van lake, Turkey: an example of development dynamics for magmatic processes. *Dokl. Earth Sci.* 433, 1031–1037.
- Lebedev, V.A., Chernyshev, I.V., Vashakidze, G.T., Gudina, M.V., Yakushev, A.I., 2012. Geochronology of Miocene volcanism in the northern part of the lesser caucasus (Erusheti highland, Georgia). *Dokl. Earth Sci.* 444, 585–590.
- Lechmann, A., Burg, J.-P., Ulmer, P., Guillong, M., Faridi, M., 2018. Metasomatized mantle as the source of mid-Miocene-quaternary volcanism in NW-Iranian Azerbaijan: geochronological and geochemical evidence. *Lithos* 304, 311–328.
- Lee, H.-Y., Chung, S.-L., Ji, J., Qian, Q., Gallet, S., Lo, C.-H., Lee, T.-Y., Zhang, Q., 2012. Geochemical and Sr-Nd isotopic constraints on the genesis of the Cenozoic Linzizong volcanic successions, southern Tibet. *J. Asian Earth Sci.* 53, 96–114.
- Li, X.-X., Li, X.-H., 2007. Formation of the 1300-km-wide intracontinental orogen and postorogenic magmatic province in Mesozoic south China: a flat-slab subduction model. *Geology* 35, 179–182.
- Lin, Y.-C., Chung, S.-L., Bingöl, A.F., Li, X.-H., Yang, J.-H., Lee, H.-Y., 2019. Late Cretaceous arc magmatism in SE Turkey: ages, geochemical variations and tectonic implications. *Goldschmidt Abstracts* 2019, 1974.
- Lin, Y.-C., Chung, S.-L., Chu, C.-H., Lee, H.-Y., Gallet, S., Wu, G., Ji, J., Zhang, Y., 2012. Geochemical and Sr-Nd isotopic characteristics of cretaceous to Paleocene granitoids and volcanic rocks, SE Tibet: petrogenesis and tectonic implications. *J. Asian Earth Sci.* 53, 131–150.
- Lin, Y.-C., Pang, K.-N., Galoyan, G., Jrashyan, R., Melkonyan, R., Lee, H.-Y., Lo, C.-H., Chung, S.-L., 2020. Age and geochemical constraints on cenozoic magmatic activity in north-western Armenia. *Lithosphere* (in review); Submitted for publication.
- Lin, Y.-C., 2020. Age and Geochemical Constraints on the Generation of Collision Zone Magmatism in Eastern Turkey [PhD thesis]. National Taiwan University (in prep.).
- Lustrino, M., Keskin, M., Mattioli, M., Lebedev, V.A., Chugaev, A., Sharkov, E., Kavak, O., 2010. Early activity of the largest cenozoic shield volcano in the circum-mediterranean area: Mt. Karacadag, SE Turkey. *Eur. J. Mineral.* 22, 343–362.
- McQuarrie, N., van Hinsbergen, D.J., 2013. Retrodeforming the Arabia-Eurasia collision zone: age of collision versus magnitude of continental subduction. *Geology* 41, 315–318.
- Neill, I., Meliksetian, K., Allen, M.B., Navasardyan, G., Kuiper, K., 2015. Petrogenesis of mafic collision zone magmatism: the Armenian sector of the Turkish-Iranian plateau. *Chem. Geol.* 403, 24–41.
- Nikogosian, I., Bracco Gartner, A., van Bergen, M., Mason, P., Van Hinsbergen, D.J., 2018. Mantle sources of recent Anatolian intraplate magmatism: a regional plume or local tectonic origin? *Tectonics* 37, 4535–4566.
- Okay, A.I., Zattin, M., Cavazza, W., 2010. Apatite fission-track data for the Miocene Arabia-Eurasia collision. *Geology* 38, 35–38.
- Pang, K.-N., Chung, S.-L., Zarrinkoub, M.H., Lin, Y.-C., Lee, H.-Y., Lo, C.-H., Khatib, M.M., 2013. Iranian ultrapotassic volcanism at ~11 Ma signifies the initiation of post-collisional magmatism in the Arabia-Eurasia collision zone. *Terra Nova* 25, 405–413.
- Pang, K.-N., Chung, S.-L., Zarrinkoub, M.H., Wang, F., Kamenetsky, V.S., Lee, H.-Y., 2015. Quaternary high-Mg ultrapotassic rocks from the Qal'eh Hasan Ali maars, southeastern Iran: petrogenesis and geodynamic implications. *Contrib. Mineral. Petrol.* 170, 27.
- Pearce, J.A., 2008. Geochemical fingerprinting of oceanic basalts with applications to ophiolite classification and the search for Archean oceanic crust. *Lithos* 100, 14–48 (f).
- Pearce, J.A., Harris, N.B., Tindle, A.G., 1984. Trace element discrimination diagrams for the tectonic interpretation of granitic rocks. *J. Petrol.* 25, 956–983.
- Pearce, J.A., Bender, J.F., De Long, S.E., Kidd, W.S.F., Low, P.J., Güner, Y., Saroğlu, F., Yilmaz, Y., Moorbat, S., Mitchell, J.G., 1990. Genesis of collision volcanism in eastern Anatolia, Turkey. *J. Volcanol. Geotherm. Res.* 44, 189–229.
- Peccerillo, A., Taylor, S.R., 1976. Geochemistry of Eocene calc-alkaline volcanic rocks from the Kastamonu area, northern Turkey. *Contrib. Mineral. Petrol.* 58, 63–81.
- Rabayrol, F., Hart, C.J., Thorkelson, D.J., 2019. Temporal, spatial and geochemical evolution of late Cenozoic post-subduction magmatism in central and eastern Anatolia, Turkey. *Lithos* 336, 67–96.
- Rudnick, R.L., Gao, S., 2014. Composition of the continental crust. In: Holland, H.D., Turekian, K.K. (Eds.), *Treatise on Geochemistry*, 2nd ed. 3. Elsevier, Oxford, pp. 1–51.
- Schleifeart, W., Darin, M., Reid, M., Umhoefer, P.J., 2018. Dynamics of episodic late Cretaceous–Cenozoic magmatism across central to eastern Anatolia: new insights from an extensive geochronology compilation. *Geosphere* 14, 1990–2008.
- Sengör, A.M.C., 1984. The cimmeride orogenic system and the tectonics of Eurasia. *Geol. Soc. Am. Spec. Pap.* 195, 181–241.
- Sengör, A., Kidd, W., 1979. Post-collisional tectonics of the Turkish-Iranian plateau and a comparison with Tibet. *Tectonophysics* 55, 361–376.
- Sengör, A.M.C., Özener, M.S., Keskin, M., Sakınç, M., Özbakır, A.D., Kayan, I., 2008. Eastern Turkish high plateau as a small Turkic-type orogen: Implications for post-collisional crust-forming processes in Turkic-type orogens. *Earth Sci. Rev.* 90, 1–48.
- Shafai Moghadam, H., Khademi, M., Hu, Z.-C., Stern, R.J., Santos, J.F., Wu, Y.-B., 2015. Cadomian (ediacaran-cambrian) arc magmatism in the ChahJām-Biarjmand metamorphic complex (Iran): magmatism along the northern active margin of Gondwana. *Gondwana Res.* 27, 439–452.
- Shaw, J.E., Baker, J.A., Menzies, M.A., Thirlwall, M.F., Ibrahim, K.M., 2003. Petrogenesis of the largest intraplate volcanic field on the Arabian plate (Jordan): a mixed lithosphere–asthenosphere source activated by lithospheric extension. *J. Petrol.* 44, 1657–1679.
- Skobeltsyn, G., Mellors, R., Gök, R., Türkelli, N., Yetirmishli, G., Sandvol, E., 2014. Upper mantle S wave velocity structure of the east Anatolian-Caucasus region. *Tectonics* 33, 207–221.
- Stampfli, G.M., Borel, G., 2002. A plate tectonic model for the Paleozoic and Mesozoic constrained by dynamic plate boundaries and restored synthetic oceanic isochrons. *Earth Planet. Sci. Lett.* 196, 17–33.
- Sun, S.-S., McDonough, W., 1989. Chemical and isotopic systematics of oceanic basalts: implications for mantle composition and processes. *Geol. Soc. Lond. Spec. Publ.* 42, 313–345.
- Tezel, T., Shibutani, T., Kaypak, B., 2013. Crustal thickness of Turkey determined by receiver function. *J. Asian Earth Sci.* 75, 36–45.
- Thompson, A.B., Connolly, J.A., 1995. Melting of the continental crust: some thermal and petrological constraints on anatexis in continental collision zones and other tectonic settings. *J. Geophys. Res. Solid Earth* 100, 15565–15579.
- Topuz, G., Candan, O., Zack, T., Yilmaz, A., 2017. East Anatolian plateau constructed over a continental basement: no evidence for the east Anatolian accretionary complex. *Geology* 45, 791–794.
- Turner, S., Sandiford, M., Foden, J., 1992. Some geodynamic and compositional constraints on "posttrogenic" magmatism. *Geology* 20, 931–934.
- Ustaömer, P.A., Ustaömer, T., Collins, A.S., Robertson, A.H., 2009. Cadomian (ediacaran-cambrian) arc magmatism in the Bitlis Massif, SE Turkey: magmatism along the developing northern margin of Gondwana. *Tectonophysics* 473, 99–112.
- Van de Zedde, D., Wortel, M., 2001. Shallow slab detachment as a transient source of heat at midlithospheric depths. *Tectonics* 20, 868–882.
- Wang, F., Jourdan, F., Lo, C.-H., Nomade, S., Guillou, H., Zhu, R., Yang, L., Shi, W., Feng, H., Wu, L., 2014. YBCs sanidine: a new standard for 40Ar/39Ar dating. *Chem. Geol.* 388, 87–97.
- Yilmaz, Y., 1993. New evidence and model on the evolution of the southeast Anatolian orogen. *Geol. Soc. Am. Bull.* 105, 251–271.
- Yilmaz, Y., Saroğlu, F., Güner, Y., 1987. Initiation of the neomagmatism in east Anatolia. *Tectonophysics* 134, 177–199.
- Zhu, D.-C., Zhao, Z.-D., Niu, Y., Dilek, Y., Wang, Q., Ji, W.-H., Dong, G.-C., Sui, Q.-L., Liu, Y.-S., Yuan, H.-L., 2012. Cambrian bimodal volcanism in the Lhasa Terrane, southern Tibet: record of an early Paleozoic Andean-type magmatic arc in the Australian proto-Tethyan margin. *Chem. Geol.* 328, 290–308.